

University of Louisville

ThinkIR: The University of Louisville's Institutional Repository

---

Electronic Theses and Dissertations

---

8-2016

# Gamma-radiation exposure alters the cardiovascular extracellular matrix.

Nicholas Allen

Follow this and additional works at: <https://ir.library.louisville.edu/etd>

 Part of the [Biomedical Engineering and Bioengineering Commons](#)

---

## Recommended Citation

Allen, Nicholas, "Gamma-radiation exposure alters the cardiovascular extracellular matrix." (2016). *Electronic Theses and Dissertations*. Paper 2483.

<https://doi.org/10.18297/etd/2483>

This Master's Thesis is brought to you for free and open access by ThinkIR: The University of Louisville's Institutional Repository. It has been accepted for inclusion in Electronic Theses and Dissertations by an authorized administrator of ThinkIR: The University of Louisville's Institutional Repository. This title appears here courtesy of the author, who has retained all other copyrights. For more information, please contact [thinkir@louisville.edu](mailto:thinkir@louisville.edu).

$\gamma$ -RADIATION ALTERS THE CARDIOVASCULAR EXTRACELLULAR MATRIX

By  
Nicholas Allen  
B.S., University of Louisville, 2015

A Thesis  
Submitted to the Faculty of the  
University of Louisville  
J.B. Speed School of Engineering  
as Partial Fulfillment of the Requirements  
for the Professional Degree

MASTER OF ENGINEERING

Department of Bioengineering

August 2016



$\gamma$ -RADIATION ALTERS THE CARDIOVASCULAR EXTRACELLULAR MATRIX

Submitted by: \_\_\_\_\_  
Nicholas Allen

A Thesis Approved On

\_\_\_\_\_  
(Date)

By the Following Reading and Examination Committee:

\_\_\_\_\_  
**Dr. Patricia Soucy, Thesis Director**

\_\_\_\_\_  
**Dr. Kevin Soucy**

\_\_\_\_\_  
**Dr. Erin Gerber**

## ACKNOWLEDGEMENTS

Thank you to my thesis director, Dr. Patricia Soucy for her guidance and extraordinary mentorship for the past 3 years. Additionally, I would like to express appreciation to the members of my thesis committee, Dr. Kevin Soucy and Dr. Erin Gerber, Dr. Robert Keynton, and the BE Department Chair, Dr. Ayman El-Baz. Thank you to Betty Nunn for her continuous help and support during the course of this project. Additionally, thank you to the past and present members of the Soucy Lab with a special thanks to: Emily Martin, Beth Farber, Katie Keynton, Ishita Jain, Dr. Archana Akalkotkar, Megan Keynton, Amanda Speller, and Jessica McQuaide Thank you to the University of Louisville's Department of Bioengineering and J.B. Speed School of Engineering for an adventurous four years as a student at the University of Louisville. Finally, thank you to my family for their constant encouragement, patience, and support.

## ABSTRACT

Ionizing radiation has been associated with various cardiovascular complications; however, the associated molecular changes from radiation exposure still remain largely uncharacterized. Alterations to the cardiovascular tissue microenvironment, i.e. the extracellular matrix (ECM), directly affect the function of integrated vascular cells, including cell adhesion, potential to form vessels, and endothelial permeability, which can promote cardiovascular pathologies. The ECM is constantly remodeled in response to stimuli, such as TGF- $\beta$ 1, which leads to excessive ECM accumulation. We hypothesize that radiation exposure will alter the cardiovascular ECM. Human Cardiac Fibroblasts (HCFs) were utilized to produce ECM as an *in vitro* model to study changes in cardiovascular ECM from exposure to 0 and 1 Gy of  $\gamma$ -radiation. We verified that the ECM produced by these cells over 7 days of culture contained collagen and fibronectin. HCFs were radiosensitive to 1 Gy of radiation, as the irradiated cells exhibited  $\gamma$ -H2AX foci. Intracellular reactive oxygen species (ROS), a known activator of latent TGF- $\beta$ 1, was increased in HCF immediately after radiation. In addition, irradiated HCF contained SMAD 2/3 in their nuclei and expressed  $\alpha$ -smooth muscle actin, which are indicative of TGF- $\beta$ 1 activation. Measurement of total ECM protein and morphology demonstrated an increase in ECM protein production and an altered ECM structure from HCF exposed to 1 Gy radiation compared to sham control. In conclusion, we demonstrate that ionizing radiation induces structural and molecular changes in cardiovascular ECM. Our data

further indicates that  $\gamma$ -irradiation activates TGF- $\beta$ 1 downstream signaling cascades, which may be a primary contributor of ECM remodeling in vascular tissue. Future studies relating ECM remodeling and cardiovascular cell function may help improve our understanding of cardiovascular risks from radiation exposure.

## TABLE OF CONTENTS

ACKNOWLEDGEMENTS	iv
ABSTRACT	v
NOMENCLATURE	vii
LIST OF TABLES	x
LIST OF FIGURES	xi
I. INTRODUCTION	
a. Radiation	1
b. Radiation Effects on the Cardiovascular Environment	3
c. ECM and Cell Signaling	4
d. Fibroblast-derived ECM	6
II. PROCEDURE	
a. Culture of fibroblasts	9
b. Seeding Cell Culture Plates to Produce ECM	9
c. Preparation of Antioxidant Cocktail	10
d. Detection of ROS in HCFs	12
e. Determining ROS Damage to HCFs	14
f. Confirming TGF- $\beta$ 1 and SMAD 2/3 Activation in HCFs	18
g. Determining Induction to Myofibroblasts	20
h. Visualizing the HCF Environment and Isolation of ECM	21
i. Examining Composition Changes in dECM	22
j. Examining Structural Changes in dECM	23
k. Quantification of Proteins Produced in dECM	24
l. Confirming Functional Endothelial Cell Changes on dECM	27
III. RESULTS AND DISCUSSION	
a. Detection of ROS in HCFs	28
b. Determining ROS Damage to HCFs	29
c. Confirming TGF- $\beta$ 1 and SMAD 2/3 Activation in HCFs	32
d. Determining Induction to Myofibroblasts	36
e. Visualizing the HCF Environment and Isolation of ECM	38
f. Examining Composition Changes in dECM	39
g. Examining Structural Changes in dECM	44
h. Quantification of Proteins Produced in dECM	46
i. Confirming Functional Endothelial Cell Changes on dECM	46
IV. CONCLUSIONS AND FUTURE WORK	48
V. REFERENCES	53
VI. CURRICULUM VITAE	56



## NOMENCLATURE

$\beta$ -radiation	Beta radiation
$\gamma$ -radiation	Gamma radiation
ROS:	Reactive Oxygen Species
AOX:	Antioxidant
ECM:	Extracellular Matrix
FN:	Fibronectin
3D:	Three Dimensional
GAGs:	Glycosaminoglycans
Col I:	Collagen I
Col III:	Collagen III
TGF- $\beta$ :	Transforming Growth Factor Beta
$\alpha$ -SMA:	Alpha Smooth Muscle Actin
HCF	Human Cardiac Fibroblasts
FBS	Fetal Bovine Serum
PS:	Penicillin/Streptomycin
(v/v)	Volume per volume
(w/v)	Weight per volume
$\mu$ g	Microgram
mg	Milligram
$\mu$ L	Microliter
mL	Milliliter
$\mu$ M	Micromolar
mM	Miliimolar
DIH <sub>2</sub> O:	Deionized Water
Gy:	Grey
PEG Catalyse:	Polyethylene Glycol Catalyse
MnTBAP:	Manganese (III) Tetrakis (4-Benzoic Acid) Porphyrin Chloride

°C	Degrees Celsius
1X – PBS	1X – Phosphate Buffer Saline
+Ca/Mg:	Plus Calcium and Magnesium
NR	Not Radiated (0 Gy)
R	Radiated (1 Gy)
NR-AOX	Not Radiated with Antioxidant
R-AOX	Radiated with Antioxidant
DCFH-DA	2', 7'-di-chloro-di-hydro-fluorescein diacetate
DMSO:	Dimethyl Sulfoxide
H <sub>2</sub> O <sub>2</sub>	Hydrogen Peroxide
DNA:	Deoxyribonucleic Acid
γ-H2AX:	Gamma H2A Histone Family, member X
FA	Formaldehyde
DAPI	4',6-Diamidino-2-Phenylindole, Dihydrochloride
NIH	National Institute of Health
AF	Alexa Flour
RT	Room Temperature
DNAse	Deoxyribonucleic Acid-ase
dECM:	Decellularized Extracellular Matrix
BCA	Bicinchoninic Acid
RIPA	Radioimmunoprecipitation
WR	Working Reagent
Cu <sup>+2</sup>	Copper (II)

## LIST OF TABLES

- TABLE 1: Experimental Conditions
- TABLE 2: Microplate Reader Settings
- TABLE 3: NIH Focinator Software Settings
- TABLE 4: RIPA Buffer Components

## LIST OF FIGURES

- FIGURE 1: Average ROS Production in NR and R HCFs
- FIGURE 2: Immunofluorescent Images of  $\gamma$ -H2AX Foci
- FIGURE 3: Focinator Thresholds of Immunofluorescent Images of  $\gamma$ -H2AX Foci
- FIGURE 4: Average  $\gamma$ -H2AX Foci per Nuclei in NR and R HCFs
- FIGURE 5: Immunofluorescent Images of TGF- $\beta$ 1 Staining
- FIGURE 6: Average Sum Intensity of TGF- $\beta$ 1 Stains per Nuclei in NR and R HCFs
- FIGURE 7: Immunofluorescent Images of SMAD 2/3 Staining
- FIGURE 8: Nikon Advanced Research ROI Selections of Immunofluorescent Images of SMAD 2/3 Staining
- FIGURE 9: Average Sum Intensity of SMAD 2/3 Stains per Nuclei in NR and R HCFs
- FIGURE 10: Immunofluorescent Images of  $\alpha$ -SMA Staining
- FIGURE 11: Average Sum Intensity of  $\alpha$ -SMA Stains per Nuclei in NR and R HCFs
- FIGURE 12: Images of All Proteins Produced in NR and R ECM
- FIGURE 13: Phase Contrast Images of ECM and dECM
- FIGURE 14: Immunofluorescent Images of FN, Col III, and Elastin Staining
- FIGURE 15: Immunofluorescent Images of FN Staining
- FIGURE 16: Nikon Advanced Research Thresholds of FN Immunofluorescent Images
- FIGURE 17: Immunofluorescent Images of Col III Staining
- FIGURE 18: Nikon Advanced Research Thresholds of Col III Immunofluorescent Images
- FIGURE 19: Immunofluorescent Images of Col I Staining
- FIGURE 20: Nikon Advanced Research Thresholds of Col I Immunofluorescent Images
- FIGURE 21: Average Volume of FN, Col III, and Col I Produced in NR and R dECM
- FIGURE 22: Average Thickness of NR and R dECM

- FIGURE 23: Anisotropic Measurements of dECM
- FIGURE 24: Average Protein Production in NR and R dECM
- FIGURE 25: Phase Contrast Images of Aortas on NR and R dECM
- FIGURE 26: Thresholded Images of Aorta Outgrowth on NR and R dECM
- FIGURE 27: Average Endothelial Cell Outgrowth on NR and R dECM

## I. INTRODUCTION

### Radiation

Exposure to ionizing radiation is an important concern in medical radiotherapy <sup>[1]</sup>, occupational exposure <sup>[2-4]</sup>, and manned space flight <sup>[5]</sup>. Different types of ionizing radiation can include Beta radiation ( $\beta$ -radiation), gamma radiation ( $\gamma$ -radiation), and high energy cosmic (HEC) radiation.  $\gamma$ -radiation can penetrate several centimeters into the skin, whereas gamma radiation ( $\gamma$ -radiation) can penetrate through the skin and into the human body. Exposure to  $\gamma$ -radiation injury can induce morphological and functional changes in noncancerous or normal tissue. Associated hazards of ionizing radiation exposure can include the development of cardiovascular diseases, carcinogenic events <sup>[6]</sup>, and congenital abnormalities <sup>[7]</sup>. Many studies have indicated a strong connection between ionizing radiation exposure and diseases; however, little is known about the pathophysiology of these phenomena. Although, it is a widely accepted fact that ionizing radiation induces an excess in exogenous reactive oxygen species (ROS). <sup>[8]</sup> These ROS species may prove to shed insight into the mechanism(s) linking ionizing radiation to a variety of diseases.

ROS refers to chemically reactive molecules (free radicals) with oxygen, such as peroxides, hydroxyl radicals, and singlet oxygens. ROS are important homeostatic molecules in non-diseased states. However, shifts in the equilibrium of ROS and ROS scavengers, known as antioxidants (AOXs), can induce oxidative stresses in cells and tissues. This oxidative stress contributes to non-

homeostatic conditions in the cell's microenvironment as well as induces DNA damage [9]. One possible way to cause this shift in equilibrium is via ionizing radiation exposure. In order to combat this equilibrium shift, cells utilize intrinsic (superoxide dismutase, catalase, glutathione, proteins, etc) and extrinsic (vitamin C and E, polyphenols, carotenoids, etc.) AOX that scavenge excessively produced ROS. [10, 11] The basic mechanism behind AOX requires that they donate electrons to ROS molecules in order to "deactivate" the free radical from causing oxidative stress. The balance of ROS and AOX activity is an ongoing process throughout the cell's entire life.

The continually changing proportions of ROS and AOXs, both intracellularly and extracellularly, create a diverse environment that makes modeling *in-vivo* conditions challenging for the accurate predictions of the risks of radiation. Previous methods of modeling human radio-sensitivities include coupling empirical evidence with radiative transfer models [12], biophysical models [13] or normal tissue complication probabilities. [14] However, these models only utilize uniform irradiation of populations at high doses whereas Ward et. al [15] has proven even significant effects can occur at low doses. **Moreover, these models do not propose any new advances in understanding the mechanisms underlying irradiation exposure and its effects on cells and tissues. Advances in cell culture methods, multidisciplinary research, and an increased clinical need for treatment of radiation induced injuries has led to a paradigm shift utilizing *in-vitro* models to**

**elucidate the biological mechanisms involved in pathophysiological conditions resulting from radiation exposure.**

### Radiation Effects on the Cardiovascular Environment

It is now recognized that the heart is susceptible to radiation exposure.<sup>[16]</sup> Many negative effects have been associated with mediastinal irradiation. Effects can include coronary artery disease, pericarditis, cardiomyopathy, valvular disease, and conduction abnormalities. Some of these effects have been observed in populations of cancer patients receiving radiation treatment<sup>[5, 17]</sup>, nuclear industry workers,<sup>[2, 4]</sup> and atomic bomb survivors<sup>[5, 17, 19]</sup>. These observations have also suggested radiation-associated cardiovascular toxicity may be progressive.<sup>[18]</sup> Atomic-bomb survivors presented premature aortic arch calcification, isolated systolic hypertension, and myocardial infarction<sup>[16, 19]</sup>. Moreover, patients receiving radiation therapy for Hodgkin's disease or left-sided breast cancer demonstrate an elevated risk of coronary heart disease, arteriosclerosis, atherosclerosis, and late-pulmonary fibrosis<sup>[20,22-26,34,35]</sup>.

Many of the aforementioned cardiovascular diseases are linked in that their pathologies show an increase in vascular stiffness.<sup>[27-29]</sup> Arterial stiffness develops from complex interactions between stable and dynamic changes involving structural and cellular components.<sup>[30-32]</sup> The main structural components of the arterial wall are two extracellular matrix (ECM) proteins: collagen and elastin. Collectively these proteins determine resilience,



compliance, and stability of the vessel wall. In diseased states, there is a dysregulation in the balance of these proteins as well as chondroitin sulfate, heparin sulfate, proteoglycans, and fibronectin (FN) <sup>[31]</sup>. Some ECM matrix proteins contain cryptic sites which are active fragments that are not normally exposed in the protein. These sites are exposed by structural or conformational changes in the ECM protein and lead to altering the structural (matrix assembly, fiber alignment, composition) & mechanical (elastic moduli, stiffness, and porosity) <sup>[33]</sup> properties of the ECM directly. These local changes can in turn cause global affects through signal transduction cascades in the function of integrated vascular cells such as endothelial cells, fibroblasts, and vascular smooth muscle cells.

### ECM and Cell Signaling

The ECM has long considered to be an inert, purely supportive, 3D network of proteins (collagenous and non-collagenous) and glycosaminoglycans (GAGs) for the cellular microenvironment. Additionally, the matrix provides a medium for cellular migration and interaction during their development, homeostasis, & regeneration. Moreover, it can provide an adhesive substrate for cells, transduce mechanical signals, regulate cell morphology and functions, such as differentiation, proliferation, and migration, and sequester and store cytokines, such as growth factors <sup>[8,10,36]</sup>. Cellular responses are tissue dependent in terms of both biochemical and biomechanical cues. Hence, understanding the

complexities surrounding ECM production, modification and remodeling, and relating these processes to physiological changes in the biochemical and biomechanical properties of the ECM, are key to determining how microenvironmental changes influence cellular responses.<sup>[37]</sup> Thus, the cell's fate, life and death, is ultimately related to and dependent on the interaction, composition, and organization of the matrix.

Each component of the ECM is unique and together the ECM components dictate the mechanical, structural, and biochemical microenvironment. For example, collagen I (Col I) fibrils provide tensile strength, collagen III (Col III) fibrils colocalize with collagen I fibrils and modulate its production, and proteoglycans, such as FN, act as adhesive substrates for cells and other matrix proteins <sup>[8,38-39]</sup>. Due to the negative charge of GAGs, they're able to alter activities of other molecules such as fibroblast growth factor, chemokines, cytokines, and those of the transforming growth factor family. <sup>[38,40]</sup>. In most connective tissue, ECM is primarily produced and organized by fibroblasts, which are constantly remodeling the ECM through the peptide growth factor regulated matrix metalloproteinases and their inhibitors.

Peptide growth factors are small proteins that regulate cell differentiation, proliferation, and apoptosis. Those of the transforming growth factor family (TGF- $\beta$ ) are molecules that are also highly involved in regulating the ECM and have been noted to play a significant role in the regulation and growth of normal, hyperplastic, and malignant prostatic epithelium. TGF- $\beta$  is a broad term

encompassing five different conformations of the protein (TGF- $\beta$ 1-5) with only TGF- $\beta$ 1-3 expressed in mammals. Specifically, TGF- $\beta$ 1 upregulates several fibrotic genes encoding fibronectin, collagens, and can activate other proteins through its type I receptor. <sup>[41]</sup> Fibroblasts secrete TGF- $\beta$ 1 as an inactive precursor as part of a protein complex where the ECM acts as a reservoir of this quiescent TGF- $\beta$ 1 <sup>[42-44]</sup>. For TGF- $\beta$ 1 to bind to its cell receptor, it must be activated by low pH, proteases, deglycosylation, plasmin, thrombospondin, integrins, radiation exposure, and ROS as well as other mechanisms <sup>[45-47]</sup>. In cancer models, ROS are extremely efficient activators of TGF- $\beta$ 1 <sup>[42,46]</sup>. This activated TGF- $\beta$ 1 is then free to interact with its associated receptor kinase on a cell membrane. Upon binding to the receptor it induces fibroblast differentiation into myofibroblasts which express  $\alpha$ -smooth muscle actin ( $\alpha$ -SMA). Myofibroblasts are associated with diseased states characterized by excessive ECM secretion. Abnormal radiation induced production of TGF- $\beta$ 1 has already been linked to cancer progression <sup>[48,49]</sup> and development of fibrosis in skin, lung, gut and liver <sup>[50]</sup>. Limited studies have explored the effects of TGF- $\beta$ 1 on cardiovascular ECM and its role in cardiovascular disease progression.

#### Fibroblast-derived ECM

Cell derived ECM scaffolds have been more recently explored as alternatives to investigating cellular and protein level changes in tissues. These ECMs are naturally produced by fibroblasts and have been shown to be similar in

composition, microstructure, biochemical properties, and bioactivity to those of the native tissues and organs. <sup>[51, 52]</sup> These ECMs are a multi-component 3D scaffold containing proteins, GAGs, and growth factors <sup>[44, 52]</sup>. The mechanical properties of cell derived ECM have been examined. Decellularized ECM (dECM) has been additionally utilized in studies in order to show its effects on cell adhesion, endothelial tubulogenesis, and other cell processes as they relate to disease progression. <sup>[53, 54]</sup> Moreover, TGF- $\beta$ 1 activation has been investigated using decellularized lung fibroblast-derived matrices <sup>[44]</sup> whereas few studies have examined non-homeostatic conditions on cell derived cardiovascular matrices and how they relate to cardiovascular disease progression.

## OBJECTIVE

We hypothesize that a human cardiac fibroblast *in vitro* model can be designed in order to investigate that  $\gamma$ -radiation exposure increases ROS, which contributes to the increased production of ECM proteins thus altering their structure and function. In order to achieve this goal, the process was threefold:

1. Develop a fibroblast cell culture model that allows for the production of a cardiovascular specific decellularized ECM
2. Examine the radiosensitivity of the fibroblast model developed in aim 1
3. Investigate radiation-induced changes to the decellularized ECM produced by cardiac fibroblast

## II. PROCEDURE

### Culturing of Fibroblasts

HCFs were obtained from Promocell and cells were cultured in Fibroblast Growth Medium 3 (Promocell) supplemented with 10% fetal bovine serum (FBS; Atlanta Biochemical) and 1% penicillin/streptomycin (PS; HyClone). All subcultures were seeded at a minimum density of 4000 cells/cm<sup>2</sup>. All experiments were conducted with HCFs less than or equal to passage 6.

### Seeding Cell Culture Plates to Produce ECM

ECM was produced on either 12 mm fibronectin coated glass coverslips (Fisherbrand) or 30 mm fibronectin coated sterile 6 well culture plates (Costar). Coverslips were sterilized by submerging each coverslip in 70% (v/v) ethanol (Decon Labs) for 30 seconds and allowed to air-dry and placed into wells of a 12 well plate. Plate wells were then treated with either 1 or 2 mL (6 or 12 well plate, respectively) of a 50 µg/µL (w/v) fibronectin (Corning) solution in deionized water (DI H<sub>2</sub>O). Once the fibronectin solution was added, the plates were then incubated for 1 hour at 37°C to allow the fibronectin solution to coat the coverslips or wells. Coating with fibronectin allowed the ECM produced by the HCFs to stay attached to the cell culture plates and coverslips post decellularization. Cells were then added to all necessary wells at 100% confluence to 6 or 12 well plates (40,000 or 200,000 cells/well, respectively) post incubation. Upon addition to cell culture plates, HCFs were cultured for 14 days

with media changes every 2 to 3 days. For ECM requiring experiments, cells were radiated with 0 or 1 Gy of  $\gamma$ -radiation and/or treated with an AOX (immediately before radiation) on day 7 using a Gammacell 40 Extractor (MDS Nordion) irradiator. For cell only requiring experiments, cells were cultured for only 3 days with radiation exposure and/or AOX treatment on day 3. 1 Gy of  $\gamma$ -radiation was used due to mandates set by the funding institution.

### Preparation of Antioxidant Cocktail

An AOX cocktail was utilized in order to reduce any ROS generated from  $\gamma$ -radiation exposure. The reduction in ROS is used to compare the effects of diminished ROS on the cells and their microenvironment (ECM) to that of the base conditions, 0 or 1 Gy of  $\gamma$  radiation. The specific concentration of the AOX cocktail used across all experiments was a mixture of a  $10^3$  Units/mL of polyethylene catalase (PEG catalase; Sigma) and a  $10 \mu\text{M}$  solution of Manganese (III) tetrakis (4-benzoic acid) porphyrin chloride (MnTBAP; Calbiochem). This AOX cocktail was used due to its structure and mechanisms. Structurally, these AOXs are able to have successful cellular uptake upon exogenous treatment. Mechanistically, the treatment of these two allow for an effective two step procedure for reduction ROS (MnTBAP reduction of ROS to  $\text{H}_2\text{O}_2$  followed by catalase reduction of  $\text{H}_2\text{O}_2$  to water).<sup>[55]</sup> PEG catalase was initially a 1 mg lyophilized powder and was reconstituted based on manufacturer specifications in a 1:1 solution of DI  $\text{H}_2\text{O}$  and Glycerol (Sigma) for a total of 2 mL. This

resulting 0.5 mg/mL solution was placed into 50  $\mu$ L aliquots and frozen at  $-20^{\circ}\text{C}$  until further use. The MnTBAP was freshly prepared before each experiment with 1 mg of MnTBAP reconstituted in 2 mL of a .01 M Tris base solution (Sigma; pH  $\sim$  7.0 -7.4; 36.3 mg Tris base dissolved in 3 mL of DI H<sub>2</sub>O). This resulting concentration of 0.5 mg/mL MnTBAP was used in obtaining the desired concentrations of the AOX cocktail needed for each experiment. To obtain the desired concentration, the AOX is mixed in the ratio of 51.3  $\mu$ L of PEG catalyse to 17.5  $\mu$ L of MnTBAP to 931.2  $\mu$ L of 1X-phosphate buffered saline (v/v) supplemented with 0.9 mM Ca<sup>+2</sup> + 0.5 mM Mg<sup>+2</sup> (1X-PBS (+Ca/Mg)) for a total of 1 mL AOX created. These ratios were adjusted throughout all experiments to obtain the necessary volume of the AOX cocktail needed. All solutions and powders were kept on ice and handled in low light due to the stability of the AOX.

The AOX cocktail is utilized in creating the 4 experimental conditions in Table 1 for all further experiments. In order to compare the effects of AOX treatment on cells and ECM production, all appropriate HCFs were introduced with the AOX cocktail immediately before irradiation.

TABLE 1: Experimental Conditions

	<b>RADIATION (0 or 1 Gy)</b>	
<b>ANTIOXIDANT (+ or -)</b>	0 Gy/No Antioxidant (NR)	1 Gy/No Antioxidant (R)
	0 Gy/Antioxidant (NR-AOX)	1 Gy/Antioxidant (R-AOX)



### Detection of ROS in HCFs

HCFs were seeded at 10,000 cells/well in 15 wells across 2 flat black 96 well plates (Costar) for a total of 30 wells seeded (3 conditions per plate, 5 replicates per condition, 2 plates designated NR and R). Based on previous work in the lab, cells were not seeded along the outer wells of each plate in order to avoid plate reader induced errors of measurements. All further work was completed in low light conditions due to the photo stability of the AOX and dyes used in the procedure.

Following one night of incubation, cell media was vacuumed up from each well and cells were washed for 5 minutes with 100  $\mu$ L of a sterile 1X-PBS +Ca/Mg solution. This mixture of PBS was used in order to avoid cell lysis or shrinkage. After 5 minutes, the PBS solution was vacuumed off and all cells were treated with 100  $\mu$ L of a 10  $\mu$ M 2', 7'-di-chloro-di-hydro-fluorescein diacetate dye (DCFH-DA; Life Technologies) in 1X-PBS +Ca/Mg and incubated at 37°C for 30 minutes. DCFH-DA is normally a lyophilized powder that was reconstituted in 8.16  $\mu$ L of DMSO to create a stock 10 mM solution. Post incubation, all wells were washed with 1X-PBS +Ca/Mg and then treated again with 100  $\mu$ L of the 1X-PBS +Ca/Mg solution. 1 mL of the AOX cocktail was created prior to use, using the methods described in the preparation of AOX section. Both plates were then taken to the irradiator and prior to radiation exposure AOX wells were aspirated of the PBS solution and treated with 100  $\mu$ L of the AOX solution. The plates were then exposed to 0 or 1 Gy of  $\gamma$  radiation.

During incubation with DCFH-DA, intracellular esterases will cleave acetate groups in the dye allowing it to “tag” oxygen species. Further esterase cleavage of lipophilic blocking groups creates a charged form of the dye allowing the dye to be retained by the cell. Upon oxidation of the cell through the generation of ROS, the dye becomes fluorescent (excitation: 492-495 nm; emission: 517-527). This fluorescence can then be measured and directly correlated to levels of ROS within the cells.

Immediately following radiation, the plates were then taken to a microplate reader and measured for fluorescent intensity using the conditions in TABLE 2.

TABLE 2: Microplate Reader Settings

<b>SHAKING</b>	<b>FLUORESCENCE INTENSITY</b>		
Duration: 30 sec.	Excitation: 485 ± 20 nm	Lag Time: 0 sec	Settle Time: 0 sec.
Amp. : 3 mm.	Emission: 535 ± 25 nm	Integration Time: 20 sec	Manual Gain
Type: Orbital	Mode: Top	# of flashes: 25	Multiple Reads Per Well: Circular

As a positive control, freshly prepared 100 µM hydrogen peroxide (H<sub>2</sub>O<sub>2</sub>; Fisher Scientific) was added to all wells of the NR plate upon completion of its read as well as after the R plate’s reading. The NR plate was replaced and read again with the addition of H<sub>2</sub>O<sub>2</sub>. Similar methods applied to the R plate. H<sub>2</sub>O<sub>2</sub> is a form ROS and was used to validate the activity of the DCFH-DA. Negative control conditions included samples with no cells with only DCFH-DA and cells

with no DCFH-DA to establish any auto-fluorescent levels. Average fluorescent values in each well were reported from the plate reader and these values were then averaged in Microsoft Excel across all conditions (n=5) to find average DCFH-DA fluorescence per condition. This level of DCFH-DA fluorescence directly relates to levels of active ROS present in HCFs. The average fluorescence for each condition was then normalized to the NR no treatment condition. The results were analyzed for equal standard deviations using statistical software (Minitab). Significance is reported by using a one-way ANOVA coupled with a Tukey post-test ( $\alpha=.05$ ). ANOVA residuals were examined to validate normal distribution.

#### Determining ROS Damage to HCFs

An excessive production of  $\gamma$ -radiation induced ROS can lead to DNA damage. <sup>[56]</sup> Cells use the phosphorylated H2AX protein ( $\gamma$ -H2AX) as an indicator for DNA damage (double strand breaks). Thus, this protein is used as a widely accepted immunofluorescent marker for DNA damage. It was used here as a marker for any damage created by an excess in ROS production by ionizing radiation.

Cells were seeded on fibronectin coated coverslips at 100% confluence. The discussed staining protocol was adapted from Wilson et. al <sup>[57]</sup>. After attachment the cells were treated with media containing 0.2% FBS for 2 days, halting proliferation of HCFs. All samples were then subjected to either 0 or 1 Gy

of  $\gamma$ -radiation and treated with AOX appropriately. Immediately following radiation, samples were fixed with a 4% formaldehyde (FA) solution (v/v) (Sigma) in DI H<sub>2</sub>O for 20 minutes. Cells were then permeabilized with a 0.1% triton solution (v/v) (Sigma) in 4% FA for 5 minutes. This permeabilization step punctures micro-holes within the cellular and nuclear membranes in order for antibodies to enter the cell and to accurately find their targeted biomolecule. All samples were then washed twice with 1X-PBS for 5 minutes each (this procedure here on out refers to "cells were washed"). After permeabilization, the cells were then treated 30 minutes with an image ITFX signal enhancer (Thermo Fisher) which allows for the mitigation of any nonspecific binding. Cells were then washed and treated with a 1:250 dilution of a primary antibody (anti- $\gamma$ -H2AX; Millipore) for 1 hour at 37°C. Once the cells were tagged with the primary antibody, samples were washed and treated with a 1:50 dilution of a secondary antibody (goat-anti mouse IgG CY3 conjugate; Millipore) for 1 hour at 37°C. Secondary antibodies are naturally fluorescent and are designed in order to tag the conjugated primary antibody, allowing for the target molecule,  $\gamma$ -H2AX in this case, to be visualized through fluorescent imaging.

Post antibody treatments, cells were then washed and treated with a 4% FA solution for 20 minutes in order to crosslink the antibodies together to allow for optimal stability of the fluorescence in the secondary antibody. Once the crosslinking step was completed, the cells were counterstained with a 1000  $\mu$ M 4', 6-diamidino-2-phenylindole-dihydrochloride (DAPI; Life Technologies)

solution for 5 minutes at room temperature (RT) in order to stain all nuclei. Cells were then washed 3 times with 1X-PBS for 5 minutes each and then washed twice with DI H<sub>2</sub>O for 10 minutes each and then mounted on 3 inch microslides (VWR) with 15  $\mu$ L of a fluorsave reagent (Millipore). Slides were imaged using a Nikon Confocal microscope at 40X magnification. Two images were taken for each coverslip. Stains for  $\gamma$ -H2AX are concentrated foci within the nuclear regions of cells. The numbers of foci per nuclei across all images was determined using Image J software and a Focinator macro created by NIH. Settings for this macro are listed in table 3. Background and front channels were selected based on the arrangement of composite images within the software. An automatic thresholding technique was used in order to mitigate subjective error. Through testing multiple thresholding processes, a Monuments design was decided upon due to its effectiveness in isolating the  $\gamma$ -H2AX foci. In order to optimally select foci and to only have complete nuclei considered, the fill holes option was selected as well as all cells on the outer edges were discarded from the analysis.

Table 3: NIH Focinator Software Settings

<b>Focinator Settings</b>	
Background Channel	Blue
Front Channel	Red
Manual Threshold	No
Mode of Threshold	Monuments
Fill Holes	Yes
Exclude Cells on Outer Edges	Yes

Nuclei were counted for each image and number of foci were counted using the find maxima setting within ImageJ. Noise levels for foci counting were set based on NR conditions and preserved through all measurements. Number of foci per nuclei were then calculated and averaged across coverslips and then averaged across all conditions (n=6, n=3 for NR-AOX) and normalized to the NR no treatment condition. The n value of 3 for NR-AOX treatment was due to limited AOX resources and is preserved through all experiments for here on out. Results were analyzed for equal standard deviations by using software (Minitab). Significance was determined by completing a one-way ANOVA coupled with a Tukey post-test ( $\alpha=.05$ ). ANOVA residuals were examined in order to verify normal distribution.

### Confirming TGF- $\beta$ 1 and SMAD 2/3 Activation in HCFs

ROS is a known activator of TGF- $\beta$ 1 and the relative amount of it was verified by staining HCFs for TGF- $\beta$ 1. Downstream signaling in response to TGF- $\beta$ 1 binding to its cell receptor can lead to translocation of SMAD 2/3 to the nucleus. SMAD 2/3 localization in the nucleus was also verified by staining HCFs for this protein in order to confirm activation of this pathway. Cells were collected in a similar fashion as in the  $\gamma$ -H2AX protocol, minus the treatment with low serum media. After 3 days of culture with media, all samples were taken to the irradiator and exposed to either 0 or 1 Gy of  $\gamma$  radiation and appropriate wells treated with AOX. Cells to be analyzed for TGF- $\beta$ 1 were then fixed immediately<sup>[58]</sup>, while SMAD 2/3 samples were fixed 6 hours post radiation.<sup>[59]</sup> A 4% FA solution in 1X-PBS was given to the cells for 20 minutes for fixation. Cells were then permeablized with a 0.1% triton solution in 4% FA for 5 minutes. All sets of coverslips were then washed twice with 1X-PBS for 5 minutes for each wash. This washing procedure will thus be referred to as "cells were washed." After the initial washings, the cells were then treated with a 1:50 dilution (anti-TGF- $\beta$ 1; Santa Cruz) or a 1:30 dilution (anti-SMAD 2/3; Santa Cruz) of a primary antibody and incubated for 1 hour at 37°C. Once the cells were tagged with the primary antibody, they were then washed and treated with a 1:30 dilution of a secondary antibody (goat anti-rabbit IgG Alexa Flour 555 conjugate (AF 555); Life Technologies) for 1 hour at 37°C. Once the secondary antibody was applied, the cells were washed and counterstained with a 1000  $\mu$ M DAPI solution for 5

minutes RT in order to stain all nuclei. Cells were then washed 3 times with 1X-PBS and then washed once with DI H<sub>2</sub>O. All coverslips were then mounted similarly as in the determining ROS damage section.

Slides were imaged using a Nikon Confocal microscope at 40X magnification. Two images for each coverslip was obtained. TGF- $\beta$ 1 slides were analyzed using Nikon Elements Advanced Research Analysis software by calculating the sum fluorescence intensity in each image. Nuclei were counted for each image and the sum intensity for each image was normalized to the number of nuclei within each image. These values were then averaged across coverslips and then averaged across all conditions (n=6, n=3 for NR-AOX). Average intensity per nuclei for all conditions were normalized to the NR no treatment condition. An f test was completed in Minitab in order to confirm equal variances. If failed, a Games-Howell post-test was used. Significance was determined by completing a one-way ANOVA coupled with a Games-Howell post-test ( $\alpha=.05$ ). ANOVA residuals were examined in order to verify normal distribution.

Analysis of SMAD 2/3 was conducted in a similar fashion with the sum intensity only calculated within the nuclear regions of the images. Nuclei were selected using the region of interest auto detect function within the software. Nuclear regions were only considered to be positive staining due to the localization of SMAD 2/3 within nuclei during times of its activation. Sum intensity per nuclei of each coverslip was then averaged across all coverslips and



then averaged across all conditions (n=6, n=3 for NR-AOX). Results were analyzed for equal standard deviations by using software (Minitab). Significance was determined by completing a one-way ANOVA coupled with a Tukey post-test ( $\alpha=.05$ ). ANOVA residuals examined confirmed normal distribution.

### Determining Induction to Myofibroblasts

The induction of HCFs to myofibroblasts was determined by staining HCFs for the myofibroblast indicator  $\alpha$ -SMA. Cells were prepared in a similar fashion as the  $\gamma$ -H2AX protocol, minus the treatment with low serum media. Appropriate samples were treated with AOX and irradiated on day 3 of culture and all sets were then fixed 24-36 hours post radiation.<sup>[60]</sup> All fixation and staining procedures were the same as in the TGF- $\beta$ 1 and SMAD 2/3 section. Cells were stained with a 1:100 dilution of a primary antibody (anti- $\alpha$ -SMA; Santa Cruz) and a 1:30 dilution of AF-555. Coverslips were mounted using the same procedure in the determining ROS damage section. Slides were imaged using the same procedure as in the TGF $\beta$ 1 and SMAD 2/3 section. Samples were analyzed similarly to TGF- $\beta$ 1 conditions with fluorescent intensity representing positive  $\alpha$ -SMA staining (n=6, n=3 for NR-AOX). Results were analyzed for equal standard deviations by using software (Minitab). An f-test was completed in Minitab in order to test for equal variances. If this test failed, a Games-Howell post used was used. Significance was determined by completing a one-way ANOVA

coupled with a Games-Howell post-test ( $\alpha=.05$ ). ANOVA residuals examined confirmed normal distribution.

### Visualizing the HCF Microenvironment and Isolation of dECM

The total composition and structure of the cell-ECM environment was visualized by staining HCFs with a 1:100 dilution of an AF 488 carboxylic acid, succinimidyl ester amino probe (Life Technologies) in order to fluorescently tag all proteins. Cells required for this experiment were acquired on fibronectin coated coverslips after 14 days of culture with radiation on day 7. All fixation, staining, and mounting procedures are similar to the confirming TGF- $\beta$ 1 and SMAD 2/3 activation in HCFs. Images taken were used as a qualitative analysis for comparing protein structure and amount for each condition.

To examine the effects of radiation on ECM remodeling, the HCFs were extracted leaving an intact ECM to examine. Appropriate cells were treated with AOX and irradiated on day 7 of culture. On day 14 of cell culture, fibronectin coated coverslips or cell culture plates for all conditions were removed of cell culture media and rinsed with 1X-PBS. A 0.1% triton X-100 solution (v/v) was then added to each well containing coated coverslips or wells. Plates were placed onto a rocking plate and left at RT for 5-7 minutes to allow dissolution of cellular membranes. Once membranes were removed, 100  $\mu$ L of a 0.1% solution of DNase I solution (Roche) was placed into the same wells and allowed to incubate for 1 hour at 37°C, or until all nuclei were no longer present.

Decellularized ECM (dECM) samples were then rinsed twice with 1X-PBS and then used for the appropriate experiments described in upcoming sections.

### Examining Composition Changes in dECM

The composition of dECM (FN, Col III and I, and elastin) was determined by staining dECMs for the all of the antibodies specific for these proteins. All fixation and staining procedures are described in all previous antibody staining sections. FN, Col III and elastin were stained on the same coverslips with 1:200, 1:10, 1:100 (respectively) dilutions of their primary antibody (anti-FN; abCAM) (anti-col III; SouthernBiotech) (anti-elastin; Santa Cruz). Samples were then treated with 1:30, 1:50, and 1:100 dilutions of AF 555, AF 488, and AF 350, respectively. (Life Technologies) Col. I was stained solely using a 1:200 dilution of its primary antibody (ant-col I; abCAM) and a 1:50 dilution of AF 488. 1 z-stack was taken for each coverslip on a Nikon confocal microscope at 40X magnification. Z-stacks allow for a 3D view of the dECM environment. These stacks were then analyzed using the Nikon analysis software in order to determine the volume of each protein present and the dECM's anisotropy.

Volume is determined by thresholding each image within the z-stack and applying this threshold to all images within the stack. This threshold selects all positive stainings of the individual proteins. Thresholds were determined by selecting the values between 0 and 4095 (representing a 12 bit color image) that maximized protein selection while minimizing noise selection. Threshold values

were preserved across all conditions. Once thresholds were applied, the volume measurement tool in the software calculates a volume of protein selected based on the threshold. A percent protein can be determined by computing the ratio of volume of the thresholded protein to that of the total volume of the stack. These values were then averaged across all coverslips and all conditions (n=6 for NR and R conditions, n =3 for NR-AOX and R-AOX conditions). Volume results were analyzed for equal standard deviations by using software (Minitab). Significance was determined for volumes by completing a one-way ANOVA coupled with a Tukey post-test. ( $\alpha=.05$ ) Residuals were analyzed in order to confirm normal distribution.

### Examining Structural Changes in dECM

Thickness and anisotropy measurements were taken in order to investigate any structural changes in dECM post  $\gamma$ -radiation exposure. Thickness measurements were reported from the collection of z stack measurements and then averaged across all coverslips measured (n = 9 for NR and R conditions, n =3 for NR-AOX and R-AOX conditions). Lower n values were again due to limited AOX resources. Average thickness for all z-stacks were then normalized to the NR no treatment condition. Thickness measurements were analyzed for equal standard deviations by using software (Minitab). Significance for thickness measurements was determined by completing a one-way ANOVA coupled with a

Games-Howell post-test ( $\alpha=.05$ ). ANOVA residuals were examined in order to verify normal distribution.

Structural organization of the dECM produced was analyzed by examining the anisotropy, or preferred direction, of the dECM fibers. Maximum intensity projections (MIPs) were taken from each z-stack which allow to view the highest level of fluorescence within all z-stack images in one composite image. Each MIP was analyzed for anisotropy using the FibrilTool macro in ImageJ. <sup>[61]</sup> This macro measures the fractional anisotropy ratio of fibers within any microscopy image based on the concept of a second order nematic tensor <sup>[62]</sup>. An area drawn around the entire image was measured for its respected anisotropic value ranging between 0 (less ordered; less restriction) and 1 (more order; more restriction). Anisotropy fractions were averaged across all conditions (n=6 for NR and R, n = 3 for NR-AOX and R-AOX) in Microsoft Excel and normalized to the NR no treatment condition. Minitab was used in order to test for equal variances. Significance is determined by using a one-way ANOVA along with a Tukey post-test ( $\alpha=.05$ ). ANOVA residuals were examined in order to verify normal distribution.

#### Quantification of Proteins Produced in dECM

The relative amount of proteins produced in ECM was determined by using a bicinchoninic acid (BCA) assay adapted from Sigma Aldrich. ECM required for this experiment for two (NR and R) conditions (5 per condition) was

obtained in 6 well plates using methods described in the production of ECM and isolation of ECM sections. Once decellularized, all ECM samples were placed on ice and solubilized in 125  $\mu$ L of a radioimmunoprecipitation (RIPA) buffer (constituents listed in table 4). Samples were rotated for 3 minutes to allow for proper distribution of RIPA buffer and then each well was scraped with a sterile cell scraper (Falcon). Samples were then allowed to sit on ice for 3 additional minutes to allow for optimal solubilization of ECM proteins. This protein-RIPA solution was collected and used in the BCA assay.

TABLE 4: RIPA Buffer Components

<b>SOLUTION</b>	<b>VOLUME</b>	<b>COMPANY</b>
50 mM Tris Base + 150 mM NaCl	9.5 mL	Sigma
100 mM Sodium Orthovanadate	200 $\mu$ L	Sigma
200 mM EDTA	100 $\mu$ L	Amresco
10% (w/v) Sodium Deoxycholate	100 $\mu$ L	Sigma
10% (v/v) Triton X- 100	100 $\mu$ L	Sigma
10 mM Leupeptin	42 $\mu$ L	Sigma
20 mg/mL Aprotinin	10 $\mu$ L	Sigma

Once the ECM was solubilized and collected, 10  $\mu$ L of samples from each condition was pipetted into a 96 well plate. 5 replicates of each sample were used. Additionally, 10  $\mu$ L of standards ranging from 0 to 10  $\mu$ g of protein were pipetted into the plate in 5 replicates. Standards were created by serial dilutions of a 1 mg/mL bovine serum albumin solution in RIPA buffer. Once all samples

were prepared in the plate a working reagent (WR) was created by mixing two separate reagents (A and B; Thermo Scientific) in the ratio of 50:1 based on the necessary amount needed for each plate. Samples and standards were mixed in the plate with a 1:8 ratio of the WR. Once mixed, the plate was incubated for 30 minutes at 37°C to allow for the WR to react with any present proteins. All plates were read for absorbance at 562 nm using a BioTek microplate reader with the conditions in table 5.

TABLE 5: Microplate Reader Settings

<b>PARAMETER</b>	<b>SETTING</b>
Assay	Quick Read
Wavelength	Single
Measure	562 nm
Plate Type	96 well

This biochemical assay measures protein concentrations within a solution. This is accomplished by using a known two-step reduction of  $\text{Cu}^{+2}$  to  $\text{Cu}^{+1}$  by proteins in alkaline mediums (the WR) using highly sensitive colorimetric detection of the  $\text{Cu}^{+1}$  cation by BCA.

Within the first step of the reaction, samples are introduced into an alkaline environment to form light blue complexes. These complexes then react with BCA to produce an intense purple-colored reaction, strongly influenced by amino acid residues, that results from the chelation of two molecules of BCA with

one  $\text{Cu}^{+1}$  ion. This purple complex is water-soluble and exhibits a strong linear absorbance at 562 nm.

Absorbance measurements obtained from the microplate reader were then averaged across each sample using Microsoft Excel. Using the standards, average absorbance was then translated into average protein amounts. Only assays resulting in less than 10% standard deviation among the standards were considered. These were then averaged across all conditions (n=5) and then normalized to the NR no treatment condition. Data obtained was then tested in Minitab for normal distribution and equal variances. Statistical significance was determined by using a t-test ( $\alpha=.05$ ). Normal distribution was verified by examining probability plots of the data collected.

#### Confirming Functional Endothelial Cell Changes on dECM

To determine if the changes in dECM alter endothelial cell (EC) function, an aorta outgrowth assay was adapted from K Soucy et. al.<sup>[63]</sup> C7BL6 control mice from another study were injected with a 0.9% physiological saline buffer and were sacrificed 10 days post injection. Aortas were surgically isolated and cut into 1-2 mm sections. A section of each aorta was placed onto NR and R dECM prepared in a 6 well plate using methods described in the isolation of dECM section. Aortas were allowed to attach to the dECM for 1 hour at 37°C. Post incubation, 3 mL of media supplemented with 0.0% FBS + 1.0% PS/Glutamine (Gibco Medium 200; Life Technologies) was added slowly to each



well, allowing the media to cover the aorta. Aortas were allowed to culture in this media for 5 days with no media change. On the fifth day, aortas were fixed using a 4% FA solution for 1 hour at RT and then imaged.

Phase contrast images were taken using a Nikon epifluorescent microscope at 10x magnification. Two images per aorta were taken (3 NR dECM, 2 R dECM). Images were thresholded using software (Nikon Elements) in order to isolate the growth area within each image by setting a threshold on the image limiting brightness (0 to 4095) and size (0 to 5  $\mu\text{m}$ ). A polygon representing the growth area was drawn using the polygon feature in the software. Area of the polygon and area of thresholded areas within the polygon were then measured using the measure function in the software. A percentage of area covered by ECs within the growth area was then calculated using Microsoft excel. Threshold values were preserved across both conditions. An average EC outgrowth area percentage was calculated using Microsoft Excel and normalized to the NR no treatment condition. Results were tested for equal variances and normal distribution using Minitab. Significance was determined by using a paired t-test ( $\alpha=0.5$ ).

### III. RESULTS AND DISCUSSION

#### Detection of ROS in HCFs

ROS levels were measured by analyzing average fluorescence of DCFH-DA in cells for all conditions. Results shown in figure 1 show a significant increase in

ROS levels by approximately 20% ( $p^* = .020$ ) between NR and R conditions as well as a significant decrease in ROS in both conditions treated with AOX when compared to their no treatment conditions ( $p^{**}$  and  $p^{***} < 0.0001$ ). In addition, we observe an increase in ROS for NR-AOX and R-AOX conditions, suggesting slightly more ROS produced in R-AOX conditions. This verifies that exposure to  $\gamma$ -irradiation increases the levels of ROS within the fibroblastic model.

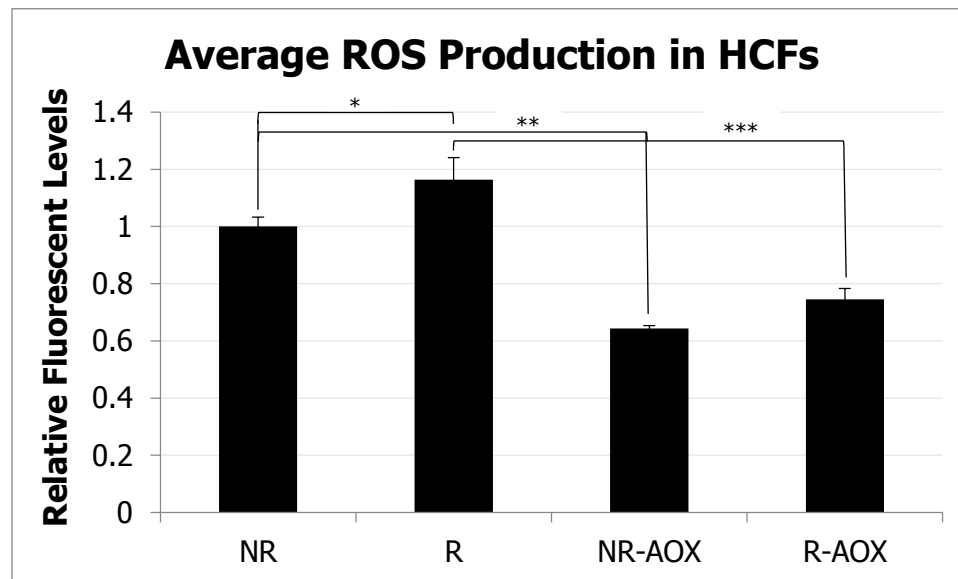


**Fig. 1: Relative fluorescent units in HCFs subjected to 0 and 1 Gy of  $\gamma$  radiation with and without AOX treatment.**

#### Determining ROS Damage to HCFs

ROS induced DNA damage to HCFs was examined by staining cells for a marker of DNA damage,  $\gamma$ -H2AX, and analyzed using computer software (Image J; Focinator). Representative images of  $\gamma$ -H2AX staining for each condition are shown in figure 2. The same images are shown in figure 3 after being ran through the focinator software. This analysis (figure 4) shows a significant

increase in  $\gamma$ -H2AX foci in radiated HCFs ( $p^* = .0004$ ). Moreover, not radiated samples treated with AOX expressed significantly decreased numbers of foci ( $p^{**} < .0001$ ) when compared to NR samples. Additionally, radiated samples treated with AOX had significantly less foci per nuclei when compared to the R condition ( $p^{***} < .0001$ ) indicating that  $\gamma$ -H2AX foci present are dependent on AOX treatment in both NR and R conditions. Moreover, we observed a nearly 2 fold increase of foci present in R-AOX conditions when compared to NR-AOX conditions, indicating further ROS dependent expression of  $\gamma$ -H2AX. The increase of ROS in radiated HCFs and the presence of  $\gamma$ -H2AX foci in HCFs following  $\gamma$ -radiation exposure indicates that HCF are radiosensitive and that both ROS and  $\gamma$ -H2AX can be minimized with AOX treatment.

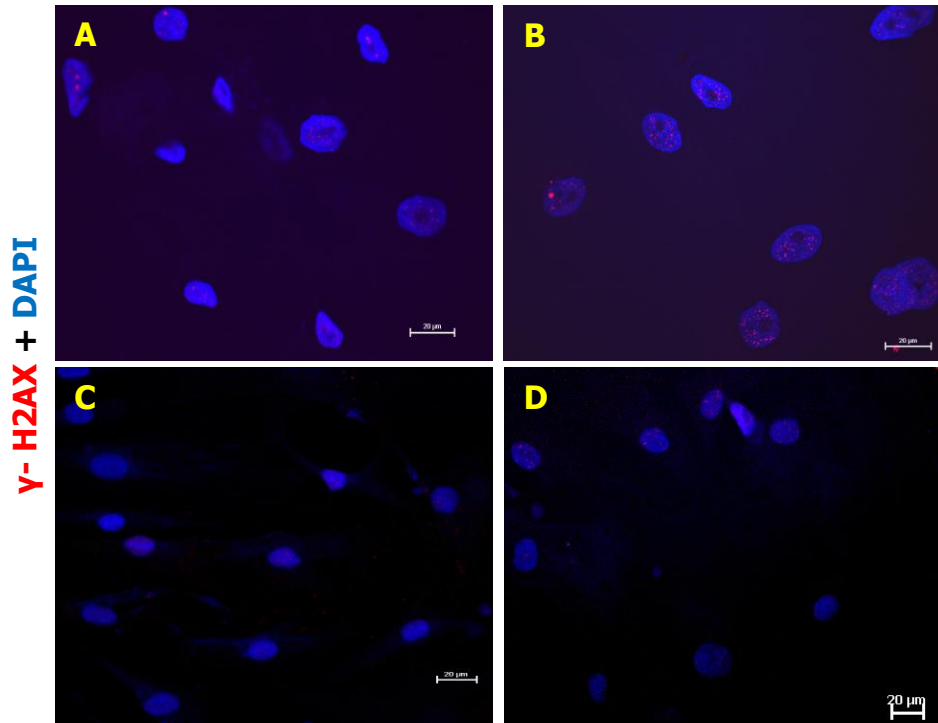


**Fig. 2: Immunofluorescent images of  $\gamma$ -H2AX foci within HCFs for all conditions: (A) No Radiation, (B) Radiation, (C) No Radiation with AOX and (D) Radiation with AOX. Scale bar indicates 20 microns.**

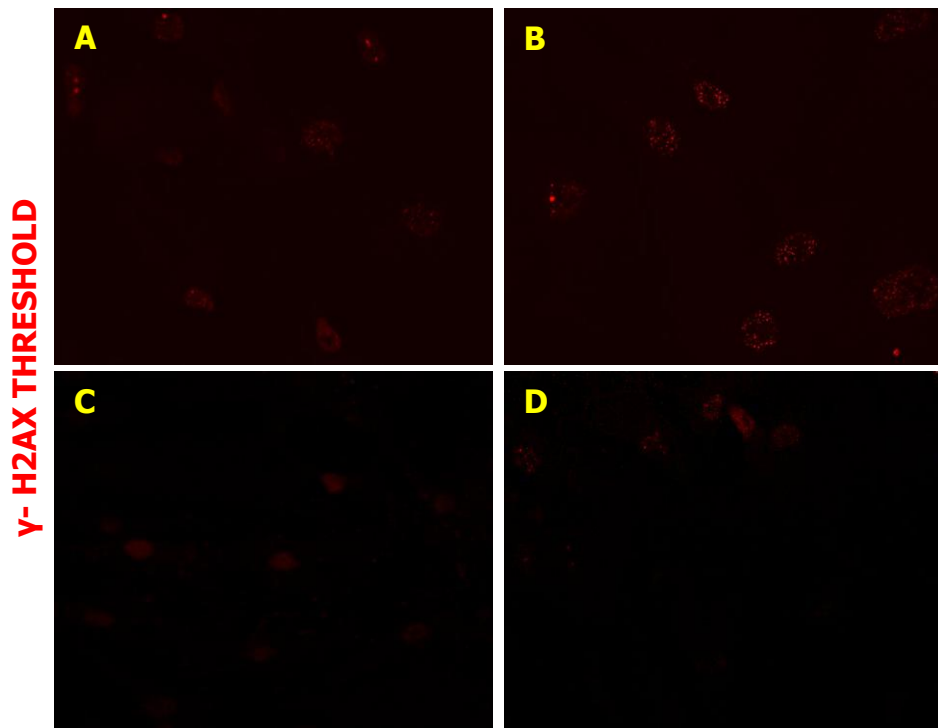


Fig. 3: Threshold results of running  $\gamma$ -H2AX images through the fociator software. (A) No Radiation, (B) Radiation, (C) No Radiation with AOX and (D) Radiation with AOX.

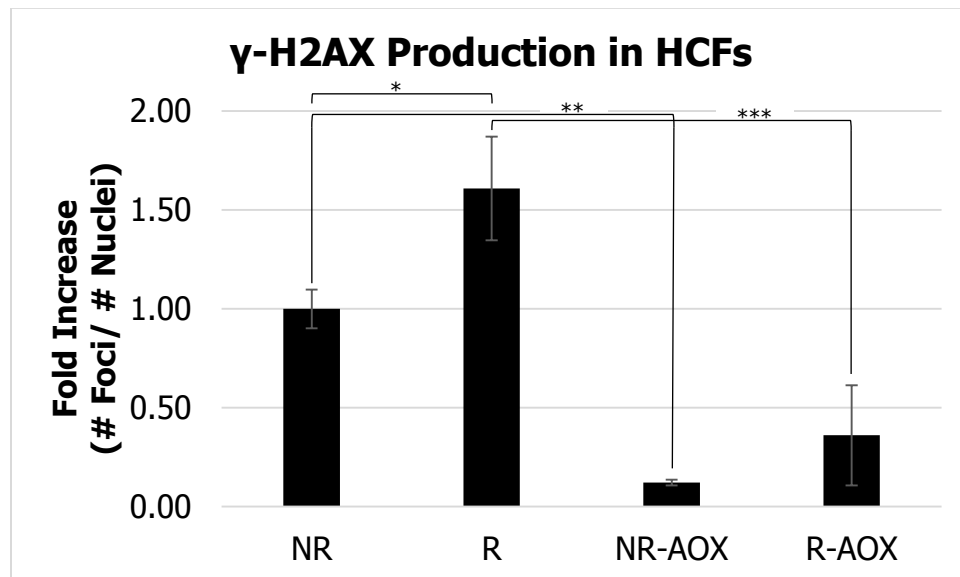
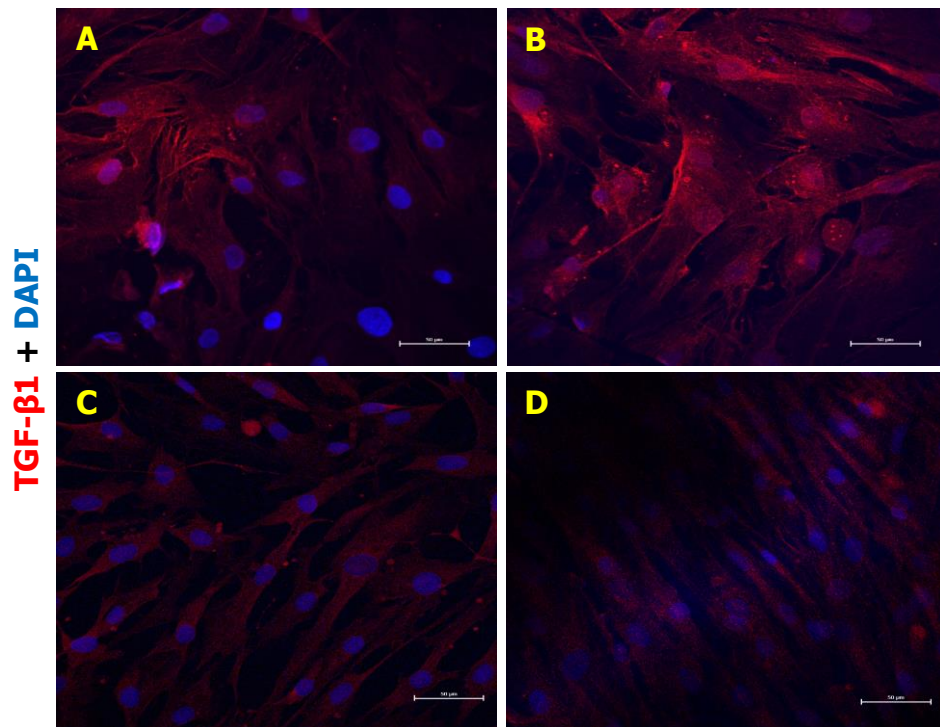


Fig. 4: Relative levels of  $\gamma$ -H2AX foci present in HCFs exposed to 0 or 1 Gy  $\gamma$ -radiation for all experimental conditions.

### Confirming TGFB and SMAD 2/3 Activation in HCFs

Relative levels of activation of TGF- $\beta$ 1, a known pro-fibrotic growth factor, was analyzed by staining for any TGF- $\beta$ 1 present in HCFs for all conditions. Representative images of TGF- $\beta$ 1 staining for each condition are shown in figure 5. Sum intensity per nuclei was measured (figure 6) and shows a significant 10-fold increase in TGF- $\beta$ 1 staining expression in radiated HCFs ( $p^* < .0001$ ). This increase is significantly attenuated in radiated samples treated with AOX ( $p^{**} < .0001$ ) while the no radiation samples treated with AOX are statistically similar to the NR no treatment condition. This trend of TGF- $\beta$ 1 production suggests that this pro-fibrotic growth factor is also a consequence of  $\gamma$ -radiation exposure and is ROS sensitive.



**Fig. 5: Immunofluorescent images of TGF- $\beta$ 1 activation within HCFs for all conditions: (A) No Radiation, (B) Radiation, (C) No Radiation with AOX and (D) Radiation with AOX. Scale bar indicates 50 microns.**

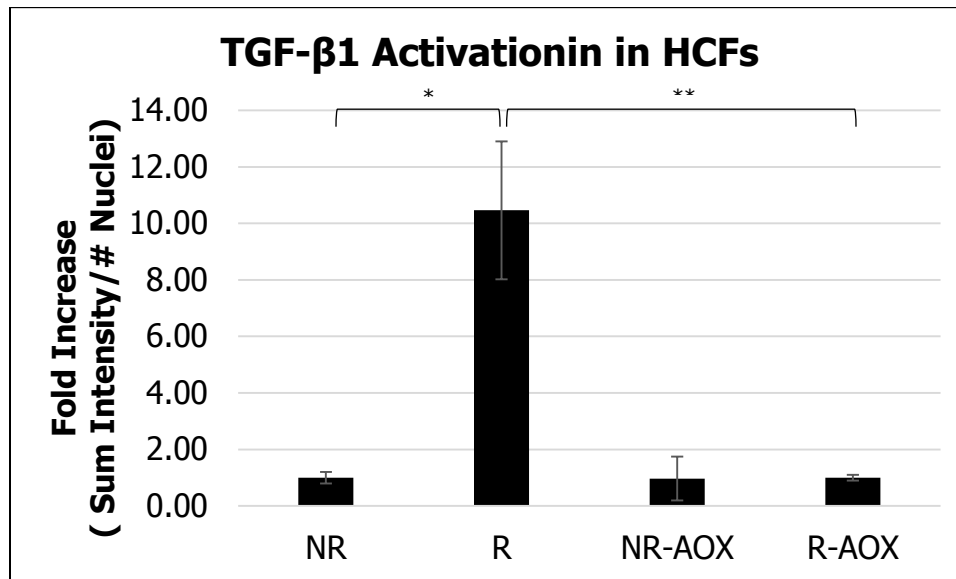


**Fig. 6: Relative levels of TGF-β1 activation in HCFs exposed to 0 or 1 Gy γ-radiation for all experimental conditions.**

SMAD 2/3 is activated in the presence of TGF-β1 and is a key contributor in the regulation of many pro-fibrotic proteins. Thus, SMAD 2/3 was stained for in HCFs for all conditions with representative images of SMAD 2/3 staining for each condition shown in figure 7. Images showing the regions of interest analyzed are shown in figure 8. Sum intensity of SMAD 2/3 staining in the nuclear regions was measured (figure 9) and shows a reluctant increase in SMAD 2/3 staining expression in radiated HCFs by 30% ( $p = .110$ ). This increase is significantly mitigated in radiated samples treated with AOX ( $p^* = .003$ ) while the NR samples treated with AOX are similar to the NR no treatment condition. Moreover, we observed a 30.8% increase of SMAD 2/3 present in R-AOX conditions when compared to NR-AOX conditions, indicating further ROS dependent expression of SMAD 2/3, This activity, similar to that of TGF-β1,

suggests that the SMAD 2/3 pro-fibrotic pathway is additionally triggered by  $\gamma$ -radiation exposure and is also ROS sensitive (most likely as a result of the altered TGF- $\beta$ 1 activity).

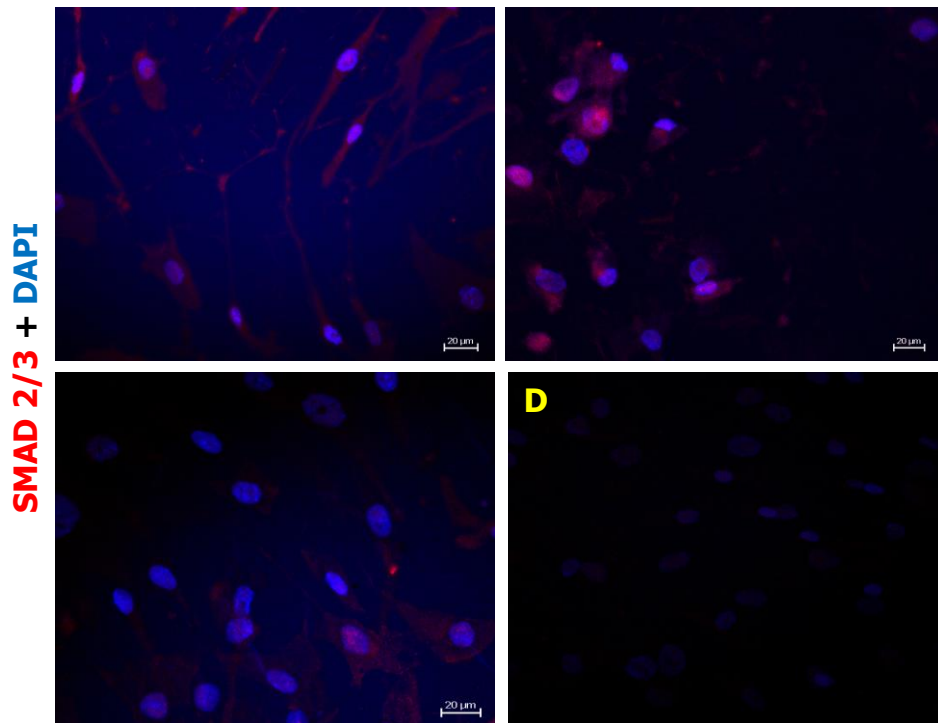


**Fig. 7: Immunofluorescent images of SMAD 2/3 activation within HCFs for all conditions: (A) No Radiation, (B) Radiation, (C) No Radiation with AOX and (D) Radiation with AOX. Scale bar indicates 20 microns.**

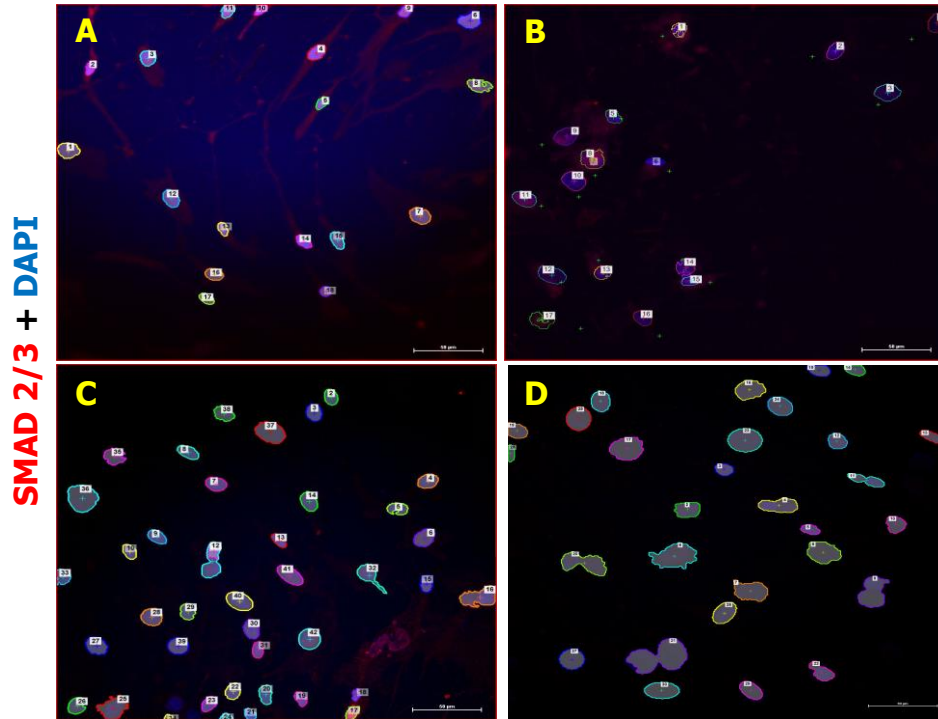


**Fig. 8:** Images with nuclear regions of interest selected for SMAD 2/3 images for all conditions: (A) No Radiation, (B) Radiation, (C) No Radiation with AOX and (D) Radiation with AOX.

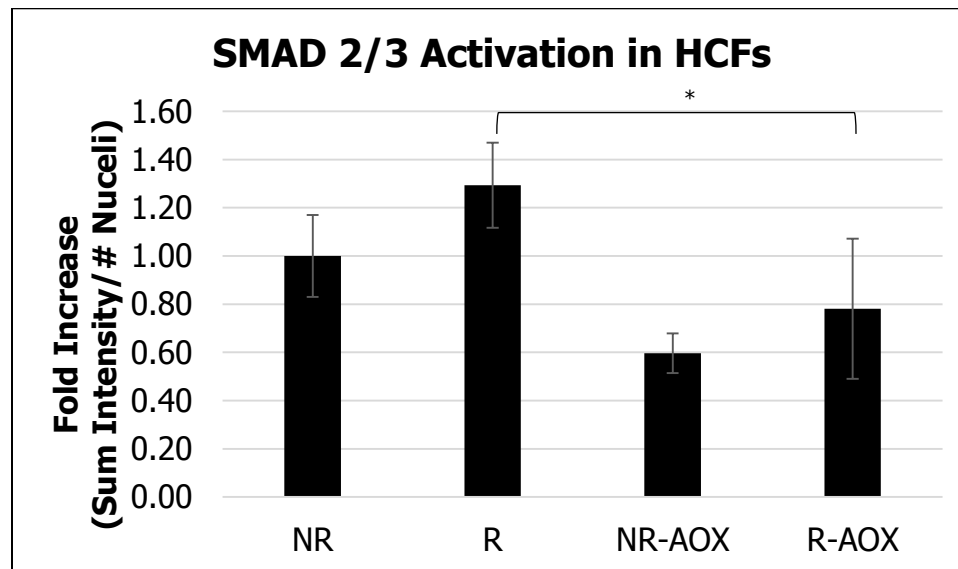


**Fig. 9:** Relative levels of SMAD2/3 activation in HCFs exposed to 0 or 1 Gy  $\gamma$ -radiation for all experimental conditions.



### Determining Induction to Myofibroblasts

Myofibroblasts are widely associated with their involvement in the excess production of proteins.  $\alpha$ -SMA is a widely accepted marker for their expression and was stained for in order to validate the presence of myofibroblasts. Representative images of  $\alpha$ -SMA staining for each condition are shown in figure 10. Sum intensity per nuclei of each image was measured and data shown in figure 11 suggests a significant 2.5 fold increase in  $\alpha$ -SMA staining expression in radiated HCFs ( $p^* = .0008$ ). Moreover, this increase is significantly decreased in radiated conditions treated with AOX ( $p^{**} < .0001$ ). This activity indicates a  $\gamma$ -radiation and ROS dependent expression of  $\alpha$ -SMA thus further suggesting that downstream effects  $\gamma$ -radiation exposure can include a fibroblasts induction to myofibroblasts and promote pro-fibrotic events.

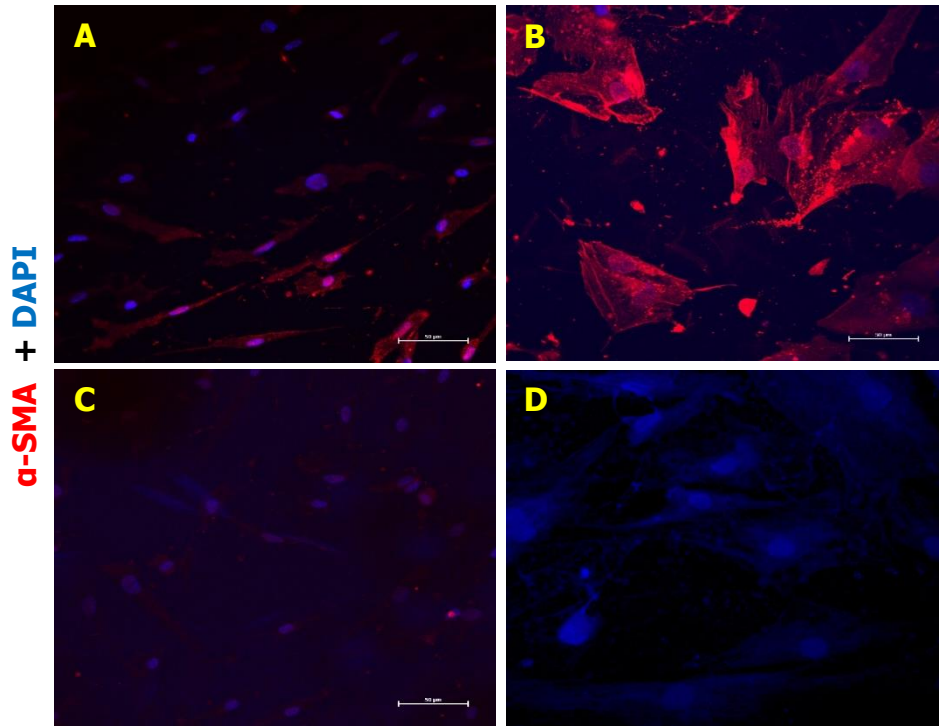


Fig. 10: Immunofluorescent images of  $\alpha$ -SMA expression within HCFs for all conditions: (A) No Radiation, (B) Radiation, (C) No Radiation with AOX and (D) Radiation with AOX. Scale bar indicates 50 microns.

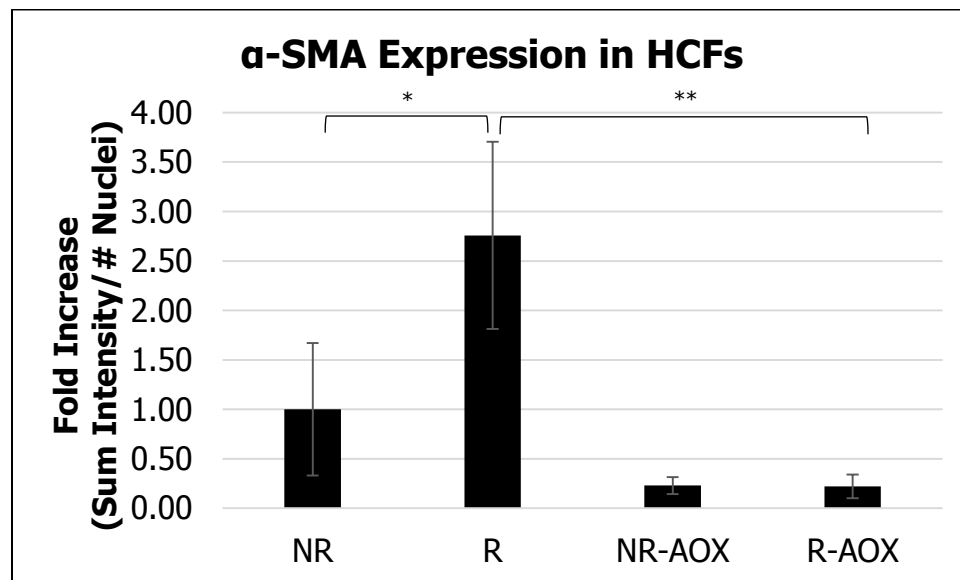
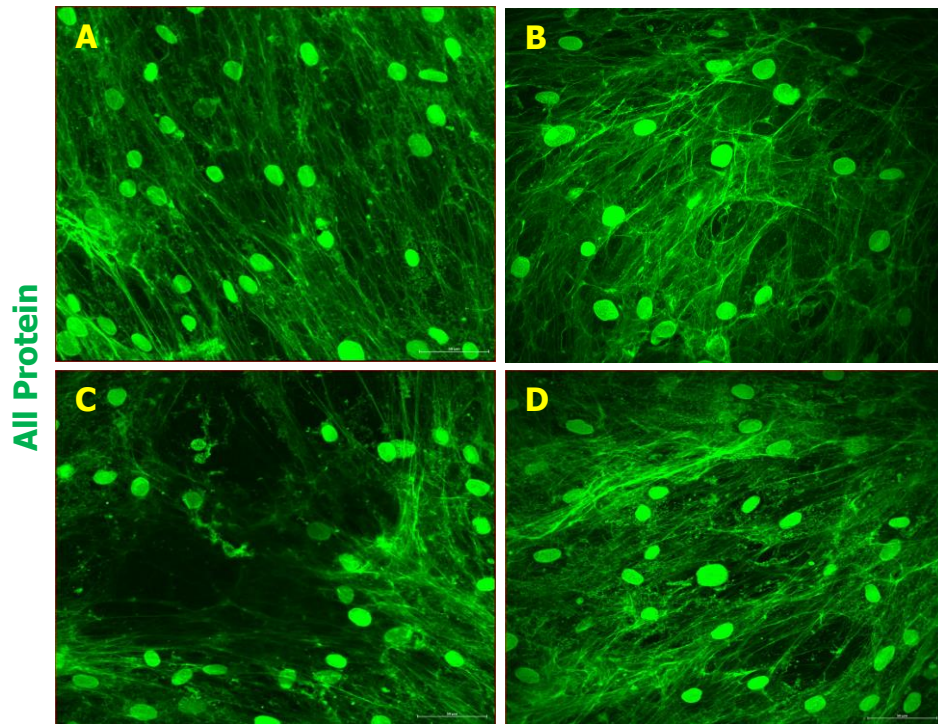


Fig. 11: Relative levels of  $\alpha$ -SMA expression in HCFs exposed to 0 or 1 Gy  $\gamma$ -radiation for all experimental conditions.

## Visualizing the HCF Microenvironment and Isolation of dECM

The HCF microenvironment is a multi-faceted combination of cells and ECM. This environment is visualized in figure 12 with MIP images for each condition. These images show a distinct structural difference in radiated samples as well as a brighter staining in radiated samples which could indicate an increased presence of protein. The ECM was decellularized (figure 13) in order to further investigate composition and structural changes to the ECM post  $\gamma$ -radiation exposure. The lack of cells in 13B indicates that the detergent based decellularization protocol is an effective tool for isolating the ECM produced by HCFs.



**Fig. 12: Representative images of the amino probe all protein stain within ECM for all conditions: (A) No Radiation, (B) Radiation, (C) No Radiation with AOX and (D) Radiation with AOX. Scale bar indicates 50 microns.**

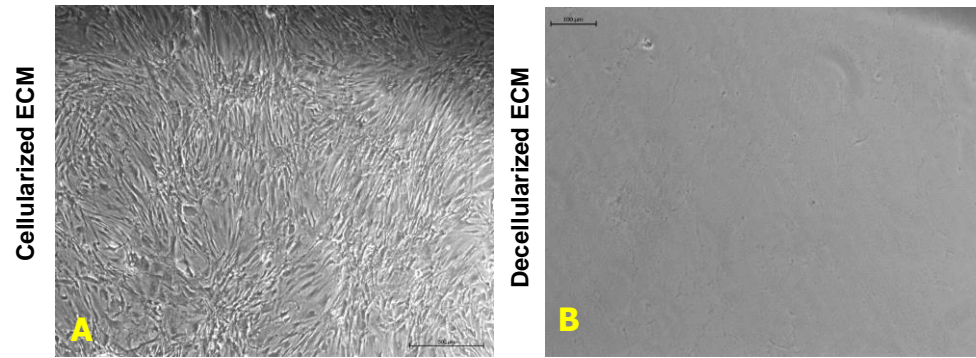


**Fig. 13: Phase contrast images of (A) cellularized extracellular matrix (ECM) and decellularized ECM (B). Scale bars indicate 100 µM.**

### Examining Composition Changes in dECM

Representative composite maximum intensity projection (MIP) images for the 3 channel ECM stained coverslips are shown in figure 14 for each condition. Individual MIP images for FN and Col III channels are shown in figures 15 and 17, respectively. MIP images for the 1 channel ECM stained coverslips are shown in fig 19 for the NR and R conditions. Thresholded images of FN, Col III, and Col. I are shown in figures 16, 18, and 20 respectively. Elastin stains and volumes are not reported due to no positive staining being observed. AOX treated collagen I conditions are not shown due to no observable difference in NR and R no treatment conditions. Relative fold increases of FN, Col III, and Col I volumes are shown in figure 21. Volume measurements show a significant 2 fold increase in FN volume in radiated HCFs ( $p^* = .0105$ ). Additionally, the same trend is observed with a 50.7% increase in FN production in R-AOX conditions when compared to NR-AOX. Furthermore, radiative groups treated with AOX show a 40% significant decrease in volume when compared to their radiated groups

( $p^{***} = .0075$ ). Fibronectin is a main ECM protein and when produced in excess, as seen in radiative environments, is indicative of fibrosis environments. Production of collagen I is decreased significantly by almost 80% between NR and R conditions ( $p^{**}=.036$ ). All other conditions for collagen I production were statistically similar. This contradictory result shown here to decrease in dECM by 75% is most likely indicating that collagen production is mandated by cells other than HCFs, most likely smooth muscle cells, and/or is modified by ECM remodeling proteins (cathepsins) post radiation exposure. No statistical difference was observed in collagen III production, although there was an observable decrease in Col III in the R condition.

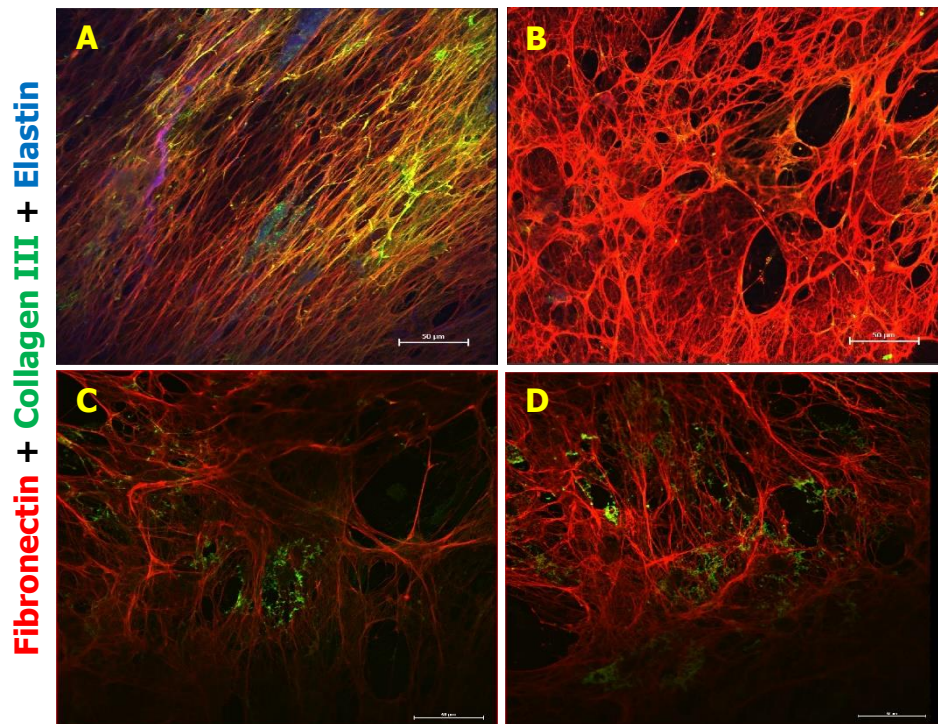


**Fig. 14: Composite maximum intensity projection images of fibronectin, collagen III, and elastin expression within dECM for all conditions: (A) No Radiation, (B) Radiation, (C) No Radiation with AOX and (D) Radiation with AOX. Scale bar indicates 50 microns.**

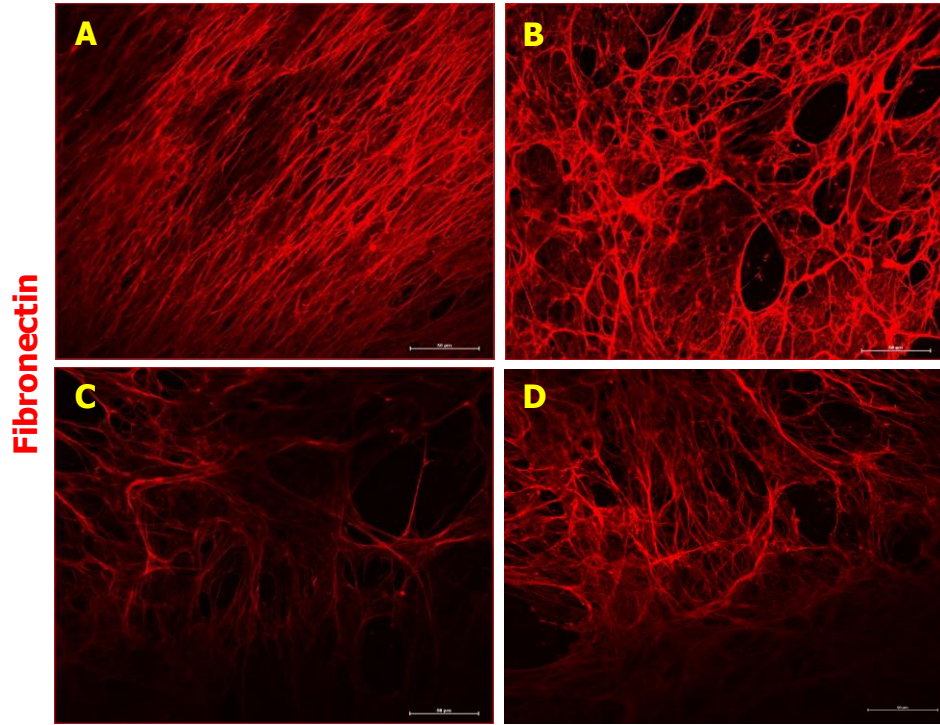


**Fig. 15: MIPs of fibronectin expression within dECM for all conditions: (A) No Radiation, (B) Radiation, (C) No Radiation with AOX and (D) Radiation with AOX. Scale bar indicates 50 microns.**

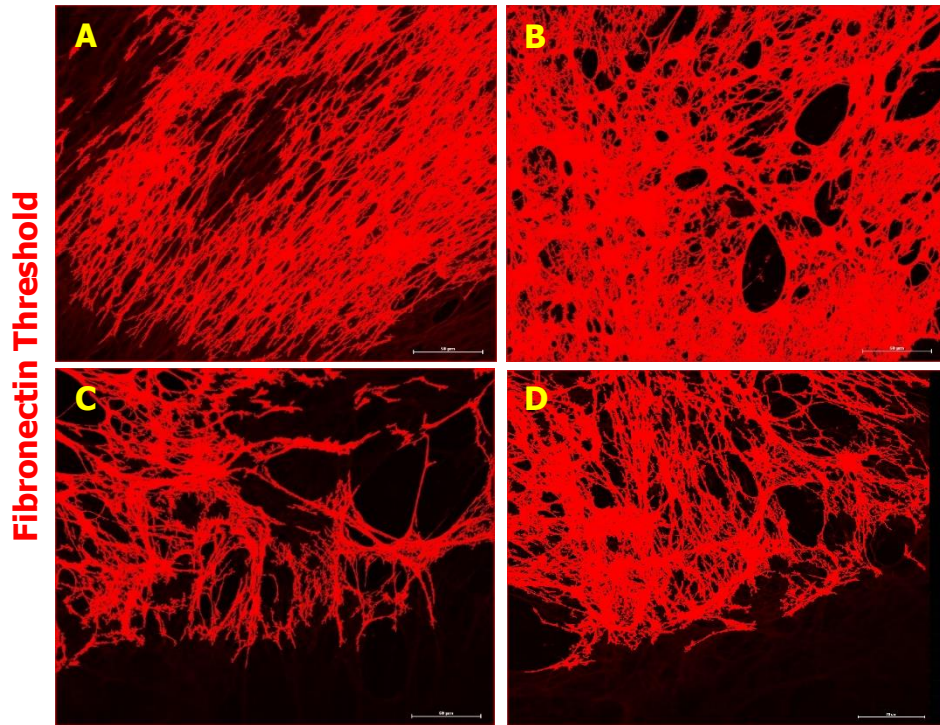


**Fig. 16: Representative thresholded images of fibronectin expression within dECM for all conditions: (A) No Radiation, (B) Radiation, (C) No Radiation with AOX and (D) Radiation with AOX. Scale bar indicates 50 microns.**

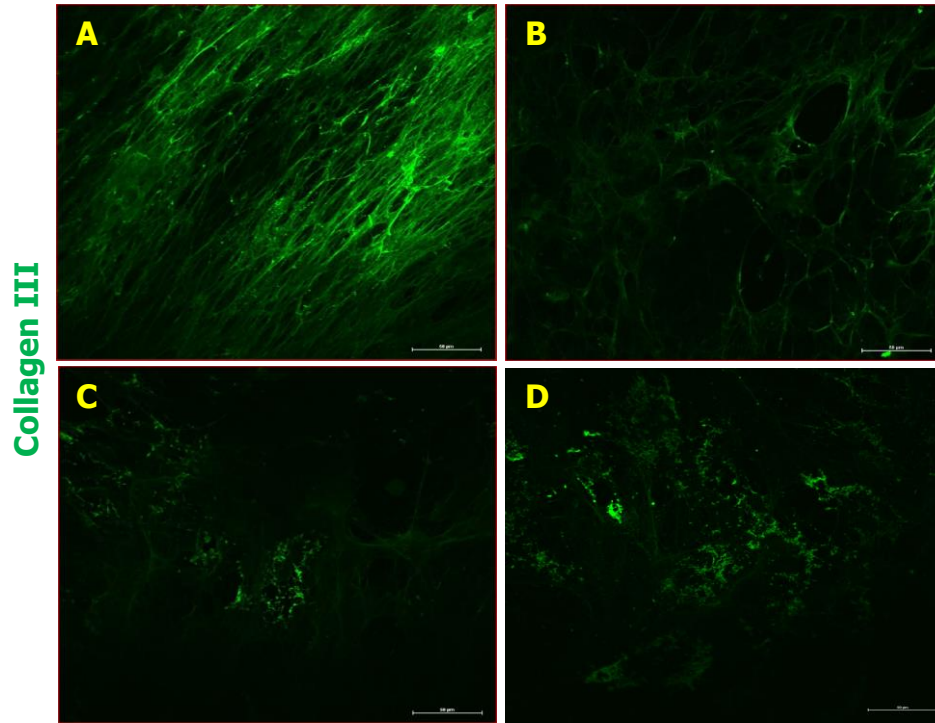


**Fig. 17: MIPs of collagen III expression within dECM for all conditions: (A) No Radiation, (B) Radiation, (C) No Radiation with AOX and (D) Radiation with AOX. Scale bar indicates 50 microns.**

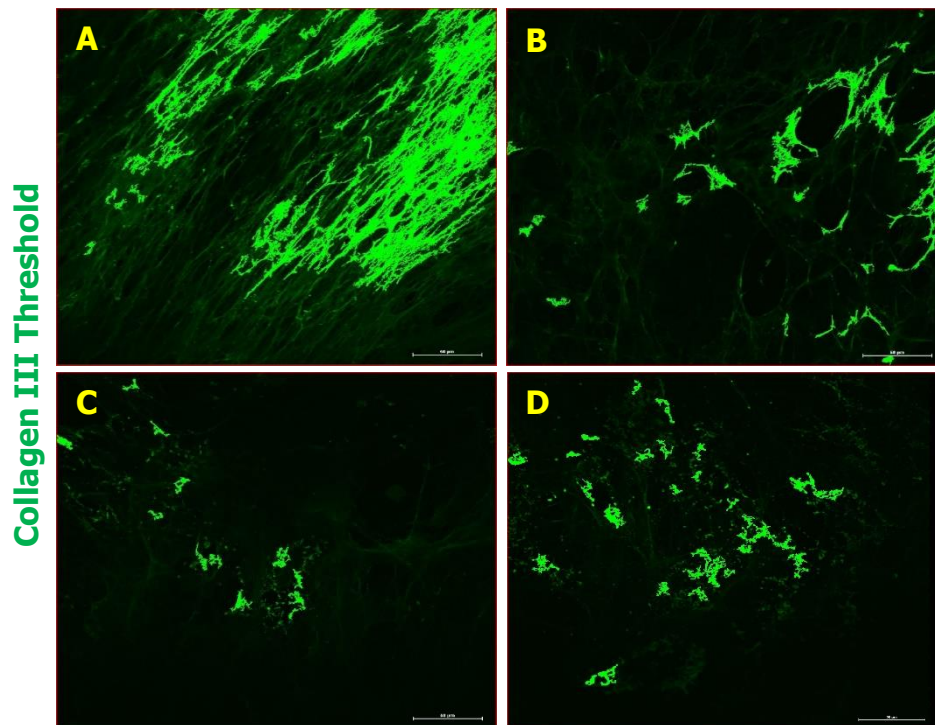


**Fig. 18: Representative thresholded images of collagen III expression within dECM for all conditions: (A) No Radiation, (B) Radiation, (C) No Radiation with AOX and (D) Radiation with AOX. Scale bar indicates 50 microns.**

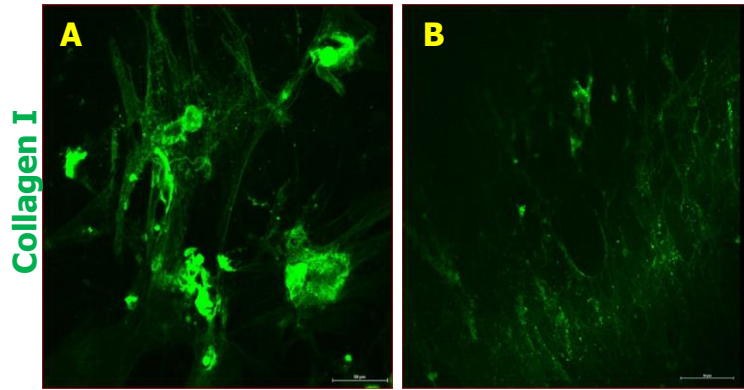


Fig. 19: Representative images for collagen I production in NR (A) and R (B) conditions within dECM. Scale bar indicates 50 microns.

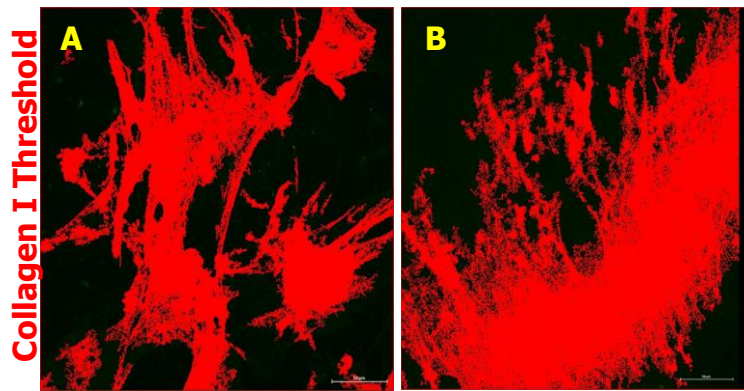


Fig. 20: Thresholded images for collagen I production in NR (A) and R (B) conditions within dECM. Scale bar indicates 50 microns.

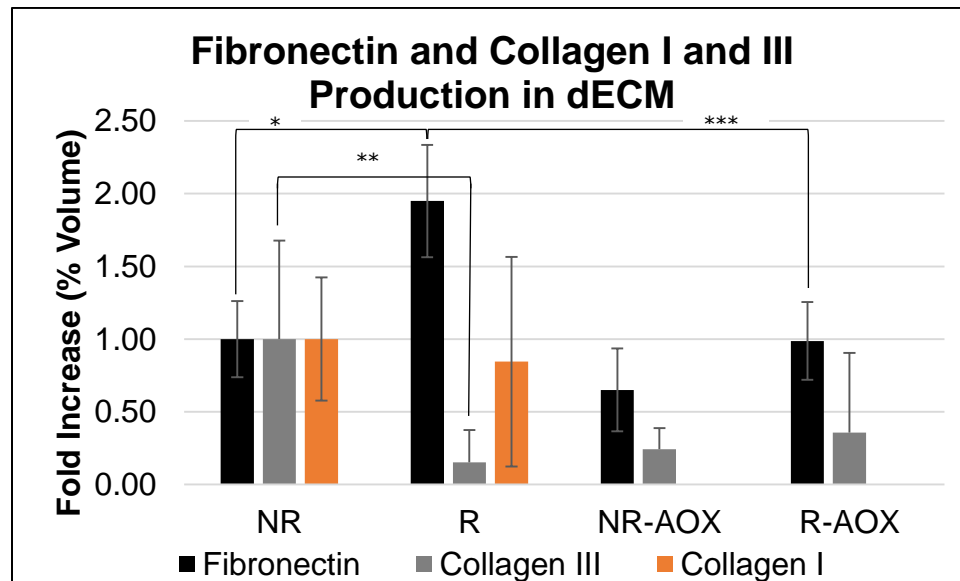


Fig. 21: Relative amounts of fibronectin (black), collagen III (gray), and collagen I (orange) production within dECM for all conditions.



### Examining Structural Changes in dECM

Structural changes to the dECM measured post  $\gamma$ -radiation exposure included the thickness and anisotropy of the dECM. Thickness measurements are presented in figure 22 and show a significant 60% increase in ECM thickness between NR and R conditions ( $p^* = .0005$ ). In addition, this increased ECM thickness is significantly decreased in R and RAOX conditions ( $p^{**} = .0059$ ). Collectively, this relationship implies protein production, and thus the thickness of ECM, is increased in response to  $\gamma$ -radiation and is dependent on the presence of ROS. Isotropic measurements are shown in figure 23 and report a significant decrease in anisotropy (1 versus .23) between NR and R conditions ( $p^* = .0004$ ) thus significantly altering the fibril structure and alignment of dECM. Moreover, in AOX treated conditions, we observe a 23% decrease in anisotropy in R-AOX conditions when compared to NR-AOX conditions. Interestingly enough though, not only is radiation a contributor to anisotropy, but data shows here that exogenous AOX treatment has a significant toll on dECM order. NR and R conditions treated with AOX are statistically less anisotropic (.4 and .3, respectively) when compared to the NR no treatment condition ( $p^{**}_{N-NA} = .0122$  and  $P^{***}_{N-RA} = .0044$ , respectively). This affect will have to be studied more in order to obtain a clearer understanding of the chemistry involved in the treatment of the AOX cocktail as well as the effect of AOX on the dECM. Nonetheless, the more significant alteration in structure observed in radiated dECM ultimately has the capacity to affect a slew of cellular and molecular

characteristics possibly leading to the phenotypical conditions observed in diseased cardiovascular states.

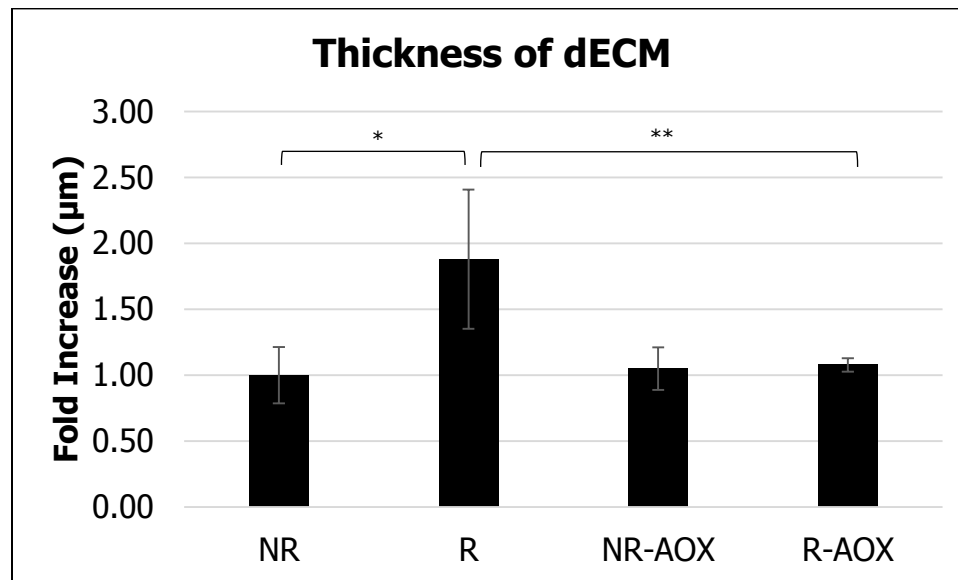


Fig. 22: Relative thickness of dECM for all conditions.

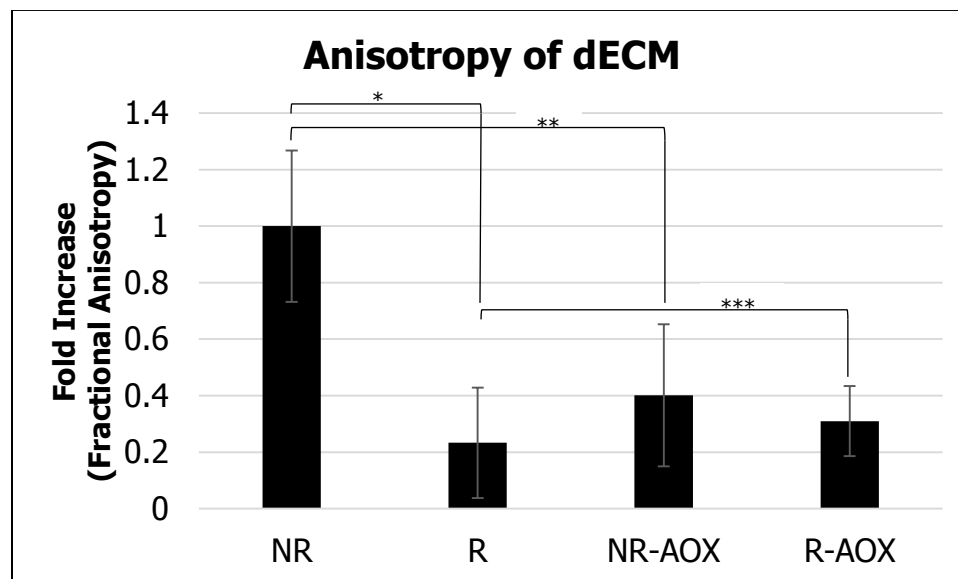
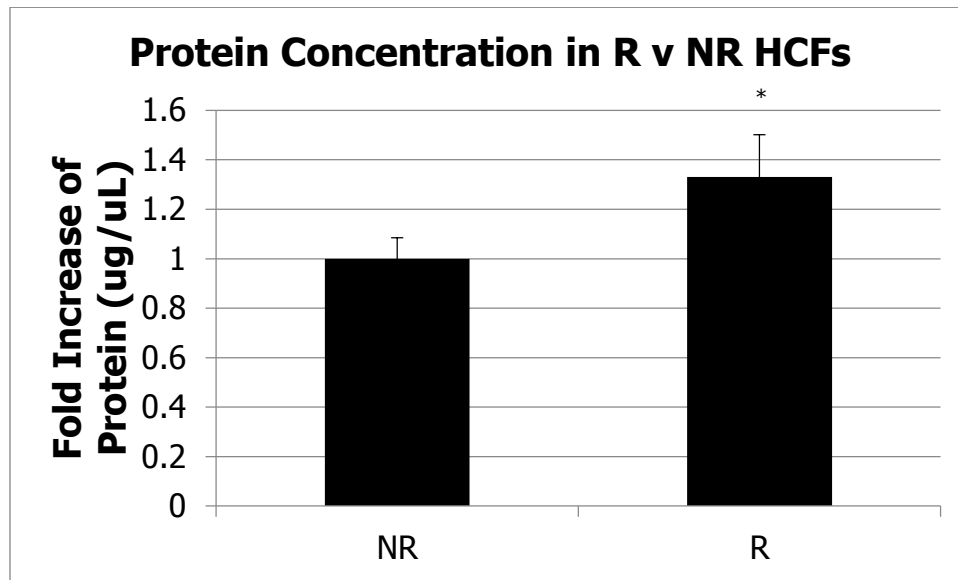


Fig. 23: Relative anisotropic values for dECM treated with 0 or 1 Gy for all experimental conditions. Values closer to 0 indicate higher levels of anisotropy.

### Quantification of Proteins Produced in dECM

Concentration of proteins produced in the dECM were quantified by using the BCA assay. Data (figure 24) expresses a significant increase of protein concentration in R samples when compared to NR samples ( $p^* = .0047$ ). This increase thus insinuates that radiation exposure contributes to an increased protein production, most likely through the action of the TGF-1 and SMAD 2/3 pro-fibrotic pathways. Moreover, this increased production of proteins is primarily done through the action of HCFs induced to myofibroblasts.



**Figure 24. Protein Production in R and NR HCF derived dECM.**

### Confirming Functional Endothelial Cell Changes on dECM

Representative images for EC outgrowth are shown in figure 25. These same images are shown thresholded in figure 26. The analysis of EC outgrowth (figure 27) reports an almost 100% observable decrease in outgrowth on R-

dECM. However, no significant changes ( $p = .499$ ) are reported notably due to variability of growth areas and low n-values.

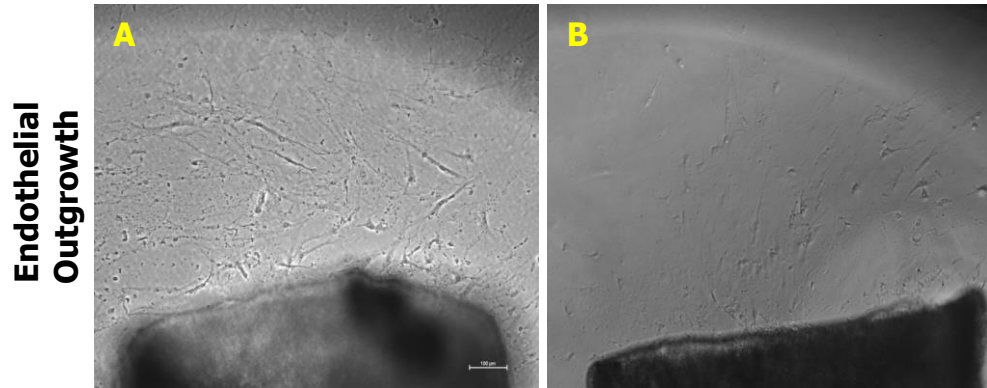


Figure 25. Respective endothelial cell outgrowth images on NR (A) and R (B) dECM.

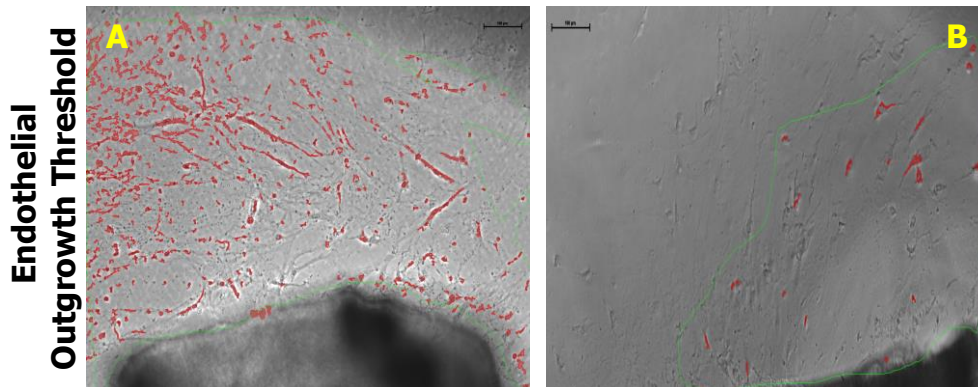
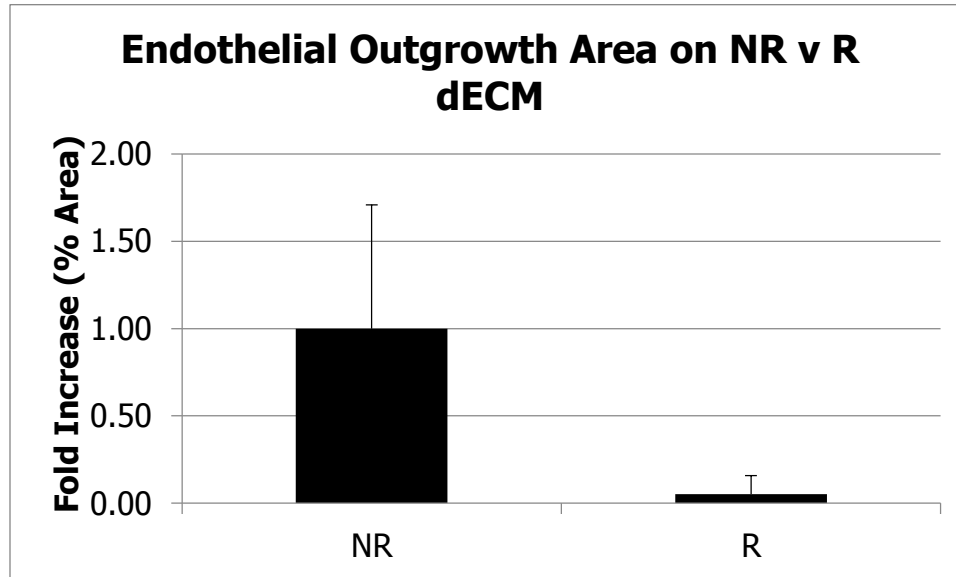


Figure 26. Respective thresholded endothelial cell outgrowth images on NR (A) and R (B) dECM



**Figure 27. Relative endothelial cell outgrowth area on NR and R dECM.**

#### IV. CONCLUSIONS AND FUTURE WORK

The first aim of this work was to develop a fibroblast cell culture model that allows for the production of a cardiovascular specific decellularized ECM. Human cardiac fibroblasts were successfully cultured and used in order to produce a cell-ECM microenvironment. This cell-ECM scaffold was then used in order to elucidate the radiative effects on cell activity in an effort to connect radiation exposure to fibrotic consequences. It was verified here that the ECM component can be decellularized successfully using detergent based methods. This HCF derived dECM was then used in order to additionally study effects of exposure to  $\gamma$ -radiation. Future studies on HCF derived dECM can supplement information regarding its composition, microstructure, biochemical properties, and bioactivity to those of its native organ

Second, it was an aim of this work to study the radiosensitivities of the fibroblastic model exposed to  $\gamma$ -radiation. We verified that exposure to  $\gamma$ -radiation increases the levels of ROS within the fibroblastic environment. ROS are known activators of pro-fibrotic signaling cascades and have already been linked to the activation and/or expression of pro-fibrotic growth factors and proteins.  $\gamma$ -H2AX foci studies completed support the idea that HCFs are radiosensitive to increased ROS levels.

ROS has been shown to efficiently activate the TGF- $\beta$  signaling pathway which is a known player in the upregulation of fibrotic genes. It achieves its goal through the activation of the SMAD 2/3 nuclear pathway which upon activation upregulates fibrotic gene transcription. Through examining both of these proteins, this work verified that both proteins are sensitive in response to ROS production thus suggesting that  $\gamma$  radiation exposure is also an activator of the TGF- $\beta$ 1 and SMAD 2/3 pathway. Increased production of fibrotic proteins, as a result of an activated SMAD 2/3 pathway, are normally characterized by the presence of myofibroblasts. We additionally verified that upon  $\gamma$ -radiation exposure there is a significant increase in  $\alpha$ -SMA expression, which is also ROS sensitive. Collectively, this HCF activity suggests that downstream effects of  $\gamma$ -radiation exposure can include pro-fibrotic events in HCFs. We thus continued our investigation into ECM level changes in response to  $\gamma$ -radiation exposure.

The ECM is the supportive framework for fibroblasts that mandate most aspects of a cells life *in-vivo* and *in-vitro*. We utilized an HCF derived ECM in

order to study the changes to the ECM function, including its composition, structure, and effects on cellular activities post  $\gamma$ -radiation exposure. Fibronectin is a key fibrotic protein that is known to be heavily influenced by the activity of TGF- $\beta$ 1. We observed an inherent increase in fibronectin production, along with increased TGF-  $\beta$ 1, and additionally report that FN production is ROS sensitive, a result strongly correlated with effects of pro-fibrotic cell signaling cascades studied here. Surprisingly, it was observed that both collagens decreased in response to radiation exposure. This contradiction suggests collagen production is mandated by more than just fibroblasts or moreover, modified post-radiation by ECM remodeling proteins, such as cathepsins, and will be investigated further in future studies. However, analysis of all proteins produced suggests a trend globally supporting an increased protein production in response to  $\gamma$ -radiation exposure. Future work will include investigating the AOX treated conditions when studying all proteins produced.

Structural studies examined the thickness and anisotropy of the ECM produced post radiation exposure. Thickness of radiated dECM was increased implying the presence of more proteins produced in radiative conditions. Additionally, in the presence of AOX the thickness of dECMs were comparable to NR groups. Collectively, this relationship also implies protein production is altered in response to  $\gamma$ -radiation and is dependent on the presence of ROS. Moreover, the structural dispersion of ECM fibrils was studied by examining anisotropy of the dECM produced. Under radiative conditions, the ECM is less

ordered, or less anisotropic thus altering the fundamental structure of ECM. Interestingly enough, not only is radiation a contributor to anisotropy, it was shown here that exogenous AOX treatment has a significant toll on dECM organization. This affect will have to be studied more in order to obtain a clearer understanding of the chemistry involved in the treatment of the AOX cocktail and its interactions with ECM molecules. Nonetheless, the alteration noted in radiated samples (samples with the least anisotropy) in structure observed is known to affect ECM characteristics possibly leading to the phenotypical conditions observed in diseased cardiovascular states.

Lastly, endothelial cell outgrowth onto ECM was examined in response to  $\gamma$ -radiation exposure in order to see if radiated ECM can alter a cells function. Although not significant, a clear result of this study was that cell migration onto ECM was hindered on radiated ECM. This is key in suggesting that the ECM plays a critical role in determining the fate of cells in its environment, both under not radiated and radiated conditions. Altered cell functions and activity are certainly known to contribute to the conditions observed in diseased cardiovascular states.

We hypothesized that an HCF *in vitro* model can be designed in order to show that  $\gamma$ -radiation exposure increases ROS which contribute to the increased production of ECM proteins thus, altering their structure and function. We investigated this task by completing radiosensitivity studies on HCFs and their ECM, seeing a general trend supporting the idea the  $\gamma$ -radiation increases protein



production and changes the molecular make up of cells and ECM. Moreover, it is shown here that  $\gamma$ -radiation exposure appears to be strongly associated with pro-fibrotic events characterized with many cardiovascular disease pathologies. This is deduced by observing increased expression or activation of  $\gamma$ -H2AX, TGF- $\beta$ 1, SMAD 2/3,  $\alpha$ -SMA, increased FN and overall protein production, and an increase in thickness and decrease in anisotropy. Clearly, this fibroblastic model has proven itself to be able to provide a novel platform to study radiation-induced changes to HCFs and ECM.

Future work will focus on improvements leading towards the progression to study *in-vivo* changes such as: (1) utilize additional quantification techniques to explore activation and production of proteins in both HCFs and dECM (2) include nuclear level investigations of pro-fibrotic gene changes in similar conditions and (3) expand the outgrowth assay to include an increased n-value with the addition of AOX treated dECM conditions.

## V REFERENCES

1. Gerber, T.C., et al., *Ionizing radiation in cardiac imaging: a science advisory from the American Heart Association Committee on Cardiac Imaging of the Council on Clinical Cardiology and Committee on Cardiovascular Imaging and Intervention of the Council on Cardiovascular Radiology and Intervention*. *Circulation*, 2009. **119**(7): p. 1056-65.
2. Cardis, E., et al., *Effects of low doses and low dose rates of external ionizing radiation: cancer mortality among nuclear industry workers in three countries*. *Radiat Res*, 1995. **142**(2): p. 117-32.
3. Ivanov, V.K., et al., *Mortality among the Chernobyl emergency workers: estimation of radiation risks (preliminary analysis)*. *Health Phys*, 2001. **81**(5): p. 514-21.
4. Muirhead, C.R., et al., *Occupational radiation exposure and mortality: second analysis of the National Registry for Radiation Workers*. *J Radiol Prot*, 1999. **19**(1): p. 3-26.
5. Cucinotta, F.A. and M. Durante, *Cancer risk from exposure to galactic cosmic rays: implications for space exploration by human beings*. *Lancet Oncol*, 2006. **7**(5): p. 431-5.
6. Jones, J. A., et al. (2010). 14.10 - Ionizing Radiation as a Carcinogen\* A2 - McQueen, Charlene A. *Comprehensive Toxicology (Second Edition)*. Oxford, Elsevier: 181-228.
7. Sankaranarayanan, K., et al. (1994). "Ionizing radiation and genetic risks. V. Multifactorial diseases: A review of epidemiological and genetic aspects of congenital abnormalities in man and of models on maintenance of quantitative traits in populations." *Mutation Research/Reviews in Genetic Toxicology* **317**(1): 1-23.
8. Denham, J. W. and M. Hauer-Jensen (2002). "The radiotherapeutic injury: a complex "wound"." *Radiother Oncol* **63**: 129-145.
9. Kuo, L.J. and L.X. Yang, *Gamma-H2AX - a novel biomarker for DNA double-strand breaks*. *In Vivo*, 2008. **22**(3): p. 305-9.
10. Finkel, T. and N.J. Holbrook, *Oxidants, oxidative stress and the biology of ageing*. *Nature*, 2000. **408**(6809): p. 239-247.
11. Ahlfors, J.E. and K.L. Billiar, *Biomechanical and biochemical characteristics of a human fibroblast-produced and remodeled matrix*. *Biomaterials*, 2007. **28**(13): p. 2183-91.
12. Polo, J., et al. (2016). "Sensitivity study for modelling atmospheric attenuation of solar radiation with radiative transfer models and the impact in solar tower plant production." *Solar Energy* **134**: 219-227.
13. Angeli, S. and T. Stylianopoulos (2016). "Biphasic modeling of brain tumor biomechanics and response to radiation treatment." *Journal of Biomechanics* **49**(9): 1524-1531.
14. Cella, L., et al. (2015). "Modeling the risk of radiation-induced lung fibrosis: Irradiated heart tissue is as important as irradiated lung." *Radiotherapy and Oncology* **117**(1): 36-43.
15. Ward, J.F. (1985). *Biochemistry of DNA lesions*. *Radiat. Res.*, **104**, S103.
16. Cucinotta, F.A., et al., *Radiation dosimetry and biophysical models of space radiation effects*. *Gravit Space Biol Bull*, 2003. **16**(2): p. 11-8.
17. Cucinotta, F. A., et al. (2001). "Space radiation cancer risks and uncertainties for Mars missions." *Radiat Res* **156**(5 Pt 2): 682-688.
18. Bouquet, F., et al., *TGFbeta1 inhibition increases the radiosensitivity of breast cancer cells in vitro and promotes tumor control by radiation in vivo*. *Clin Cancer Res*, 2011. **17**(21): p. 6754-65.
19. Reitz, G., et al. (1993). "Dosimetry in the space radiation field." *Clin Investig* **71**(9): 710-717.
20. Wilson, P. F., et al. (2010). "Inter-individual variation in DNA double-strand break repair in human fibroblasts before and after exposure to low doses of ionizing radiation." *Mutat Res* **683**(1-2): 91-97.
21. Zeitlin, C., et al. (2013). "Measurements of energetic particle radiation in transit to Mars on the Mars Science Laboratory." *Science* **340**(6136): 1080-1084.
22. Wipff, P.J., et al., *Myofibroblast contraction activates latent TGF-beta1 from the extracellular matrix*. *J*
23. Stewart, J.R. and L.F. Fajardo, *Radiation-induced heart disease. Clinical and experimental aspects*. *Radiol Clin North Am*, 1971. **9**(3): p. 511-31.

24. Hancock, S.L., M.A. Tucker, and R.T. Hoppe, *Factors affecting late mortality from heart disease after treatment of Hodgkin's disease*. JAMA, 1993. **270**(16): p. 1949-55.
25. Hayashi, T., et al., *Radiation dose-dependent increases in inflammatory response markers in A-bomb survivors*. Int J Radiat Biol, 2003. **79**(2): p. 129-36.
26. Kodama, K., K. Mabuchi, and I. Shigematsu, *A long-term cohort study of the atomic-bomb survivors*. J Epidemiol, 1996. **6**: p. S95-S105
27. Shimizu, Y., et al., *Studies of the mortality of atomic bomb survivors. Report 12, part II. Noncancer mortality: 1950-1990*. Radiat Res, 1999. **152**: p. 374-389.
28. Preston, D.L., et al., *Studies of mortality of atomic bomb survivors. Report 13: Solid cancer and noncancer disease mortality: 1950-1997*. Radiat Res, 2003. **160**(4): p. 381-407.
29. Bilora, F., et al., *Are Hodgkin and non-Hodgkin patients at a greater risk of atherosclerosis? A follow-up of 3 years*. Eur J Cancer Care (Engl), 2010. **19**(3): p. 417-9.
30. Hovingh, G. K., et al. (2004). "A novel apoA-I mutation (L178P) leads to endothelial dysfunction, increased arterial wall thickness, and premature coronary artery disease." Journal of the American College of Cardiology **44**(7): 1429-1435.
31. Ziemann, S. J., et al. (2005). "Mechanisms, Pathophysiology, and Therapy of Arterial Stiffness." Arteriosclerosis, Thrombosis, and Vascular Biology **25**(5): 932-943.
32. Stewart, F.A., S. Hoving, and N.S. Russell, *Vascular damage as an underlying mechanism of cardiac and cerebral toxicity in irradiated cancer patients*. Radiat Res, 2010. **174**(6): p. 865-9.
33. Soucy, P. A. and L. H. Romer (2009). "Endothelial cell adhesion, signaling, and morphogenesis in fibroblast-derived matrix." Matrix Biol **28**(5): 273-283.
34. Chargari, C., et al., *Complications of thoracic radiotherapy*. Presse medicale, 2013. **42**(9 Pt 2): p. e342-51.
35. Westbury, C.B. and J.R. Yarnold, *Radiation fibrosis--current clinical and therapeutic perspectives*. Clinical oncology, 2012. **24**(10): p. 657-72.
36. Boothe, D.L., et al., *Transforming growth factor beta-1 (TGF-beta1) is a serum biomarker of radiation induced fibrosis in patients treated with intracavitary accelerated partial breast irradiation: preliminary results of a prospective study*. International journal of radiation oncology, biology, physics, 2013. **87**(5): p. 1030-6.
37. Hoganson, D. M., et al. (2010). "The retention of extracellular matrix proteins and angiogenic and mitogenic cytokines in a decellularized porcine dermis." Biomaterials **31**(26): 6730-6737.
38. Munakata, M., et al., *Higher brachial-ankle pulse wave velocity is associated with more advanced carotid atherosclerosis in end-stage renal disease*. Hypertens Res, 2005. **28**(1): p. 9-14.
39. Ceravolo, R., et al., *Pulse pressure and endothelial dysfunction in never-treated hypertensive patients*. J Am Coll Cardiol, 2003. **41**(10): p. 1753-8.
40. Meaume, S., et al., *Aortic pulse wave velocity predicts cardiovascular mortality in subjects >70 years of age*. Arterioscler Thromb Vasc Biol, 2001. **21**(12): p. 2046-50.
41. Fitch, R.M., et al., *Nitric oxide synthase inhibition increases aortic stiffness measured by pulse wave velocity in rats*. Cardiovasc Res, 2001. **51**(2): p. 351-8.
42. Jadhav, U.M. and N.N. Kadam, *Non-invasive assessment of arterial stiffness by pulse-wave velocity correlates with endothelial dysfunction*. Indian Heart J, 2005. **57**(3): p. 226-32.
43. Wilkinson, I.B., S.S. Franklin, and J.R. Cockcroft, *Nitric oxide and the regulation of large artery stiffness: from physiology to pharmacology*. Hypertension, 2004. **44**(2): p. 112-116.
44. Giannone, G. and M.P. Sheetz, *Substrate rigidity and force define form through tyrosine phosphatase and kinase pathways*. Trends Cell Biol, 2006. **16**(4): p. 213-23.
45. Parsons, J.T., *Focal adhesion kinase: the first ten years*. J Cell Sci, 2003. **116**(Pt 8): p. 1409-16.
46. Sawada, Y., et al., *Force sensing by mechanical extension of the Src family kinase substrate p130Cas*. Cell, 2006. **127**(5): p. 1015-26.
47. Vuori, K., *Integrin signaling: tyrosine phosphorylation events in focal adhesions*. J Membr Biol, 1998. **165**(3): p. 191-9.
48. Goh, K.L., J.T. Yang, and R.O. Hynes, *Mesodermal defects and cranial neural crest apoptosis in alpha5 integrin-null embryos*. Development, 1997. **124**(21): p. 4309-19.
49. Joshi, P., et al., *Endothelial cells adhere to the RGD domain and the fibrinogen-like terminal knob of tenascin*. J Cell Sci, 1993. **106** ( Pt 1): p. 389-400.

50. Rozario, T. and D.W. Desimone, *The extracellular matrix in development and morphogenesis: A dynamic view*. Dev Biol, 2009.
51. Daley, W.P., S.B. Peters, and M. Larsen, *Extracellular matrix dynamics in development and regenerative medicine*. J Cell Sci, 2008. **121**(Pt 3): p. 255-64.
52. Hynes, R.O., *Fibronectins*. 1990, New York: Springer-Verlag. xv, 546 p.
53. Miura, T., et al., *Decorin binds myostatin and modulates its activity to muscle cells*. Biochem Biophys Res Commun, 2006. **340**(2): p. 675-80.
54. Du, S. and M.H. Barcellos-Hoff, *Tumors as organs: biologically augmenting radiation therapy by inhibiting transforming growth factor beta activity in carcinomas*. Semin Radiat Oncol, 2013. **23**(4): p. 242-51.
55. Soucy, K. G., et al. (2010). "Dietary inhibition of xanthine oxidase attenuates radiation-induced endothelial dysfunction in rat aorta." Journal of Applied Physiology **108**(5): 1250-1258.
56. Kuo, L.J. and L.X. Yang, *Gamma-H2AX - a novel biomarker for DNA double-strand breaks*. In Vivo, 2008. **22**(3): p. 305-9.
57. Wilson, P. F. (2010). "Inter-individual variation in DNA double-strand break repair in human fibroblasts before and after exposure to low doses of ionizing radiation." Mutation Research/Fundamental and Molecular Mechanisms of Mutagenesis: 91-97.
58. Koli, K., et al., *Latency, activation, and binding proteins of TGF-beta*. Microsc Res Tech, 2001. **52**(4): p. 354-62.
59. Warner, D.R., et al., *Identification of three novel Smad binding proteins involved in cell polarity*. FEBS Lett, 2003. **539**(1-3): p. 167-73.
60. Yu, J., et al., *MnTBAP Therapy Attenuates Renal Fibrosis in Mice with 5/6 Nephrectomy*. Oxidative Medicine and Cellular Longevity, 2016. **2016**: p. 10.
61. Boudaoud, A., et al., *FibrilTool, an ImageJ plug-in to quantify fibrillar structures in raw microscopy images*. Nat. Protocols, 2014. **9**(2): p. 457-463.
62. Nijel J. Mottram, C.J.P.N., *Introduction to Q-tensor Theory* Cornell University Library, 2014.
63. Soucy, K.G., et al., *Single exposure to radiation produces early anti-angiogenic effects in mouse aorta*. Radiat Environ Biophys, 2010. **49**(3): p. 397-404.

## CURRICULUM VITAE

**Nicholas C. Allen**

Brandenburg, KY 40108 | [allnnc010@me.com](mailto:allnnc010@me.com)

### **EDUCATION**

<b>M.Eng in Bioengineering</b>	J.B Speed School of Engineering UofL	August 2016
<b>B.S. in Bioengineering</b> <i>summa cum laude</i> <b>Minor of Pure Mathematics</b>	J.B. Speed School of Engineering UofL	May 2015
<b>Associate of Science with High Distinction</b>	Elizabethtown Community and Technical College	May 2012

### **WORK EXPERIENCE**

<b>Undergraduate Co-op: Tissue Engineering and Lab of Biomimetics</b>	<b>University of Louisville</b>	<b>May 2013 – Present</b>
---	-------------------------------------	-------------------------------

- Collaborate in a cross functional research team doing tissue engineering research for animals and humans
- Utilize laboratory equipment in order to characterize tissue samples
- Analyze test data via statistical techniques
- Make bi-weekly progress presentations to the entire team
- Learn essential lab skills such as immunofluorescence, microscopy, cell culture and sterile techniques
- Employee in Summer 2013, have continued to volunteer in lab with progressing undergraduate research into M.Eng thesis

<b>Undergraduate Co-op: Regenerative Medicine</b>	<b>Texas Heart Institute</b>	<b>January 2015 – May 2015</b>
---	----------------------------------	------------------------------------

- Explored with a diverse team environment the decellularization of various tissues for regenerative medicine applications
- Learned surgical isolation techniques used for various tissue harvesting
- Independently designed experimental plan for particular project given
- Recorded weekly status updates and notes on project as well as presented status presentations to lab during placement

## **WORK EXPERIENCE CONTINUED**

**Undergraduate Co-op:  
Garbett Lab of Structural Biology**

**James Graham  
Brown Cancer  
Center**

**May 2014 –  
August 2014**

- Investigated protein-protein interaction of melanoma and other diseases
- Learned essential analytical lab techniques such as Size Exclusion Chromatography, BCA assay, DSC analysis, and SDS gel electrophoresis
- Used Origin 7.0 (data analysis software) to analyze large quantities of experimental data
- Present daily updates to research team
- Manuscript currently in progress

**REACH Academic Assistance:  
Supplemental Instruction Leader,  
Learning Resource Center Tutor,  
Peer Supervisor and Master Tutor**

**University of  
Louisville**

**January 2013 –  
Present**

- Gave instruction for ENGR 330: Linear Algebra, ENGR 307: Numerical Methods, BIO 102: Intro to Biology, BIO 240: Unity of Life, BIO 229: Anatomy and Physiology, and Statistics in MATH, BIO, IE, and NURS disciplines
- Coordinate lessons for additional instruction in conjunction with professor
- Construct informative and in depth handouts of material in order to test student's understanding of the material
- Evaluate other session leaders in job progress throughout the semester
  - Conducted multiple observations throughout the semester
  - Perform regular screenings of material distributed adheres to tutor guidelines
  - Enter in attendance data of each tutor's sessions
  - Give final evaluation of tutor's performance
- Conduct critical thinking assessment of each small group tutoring session to evaluate tutee's progression

## **PROFESSIONAL ACCOMPLISHMENTS**

### **Poster Presentations:**

- Nick Allen, Kevin Soucy, Robert Keynton, Patricia Soucy. **"Cardiovascular Extracellular Matrix Remodeling due to Ionizing Radiation Exposure"** ASGSR Annual Meeting: Fall 2015
- Nick Allen, Eric Chau, Luiz Sampaio, Andrea Gobin, Doris Taylor. **"Construction of CAB Graft Using Decellularization and Recellularization Techniques"** BMES Annual Meeting: Fall 2015
- Nick Allen, Mary B. Hatch, Alagammai Kaliappan, Clarke Miller, & Nichola Garbett. **"Exploring the Melanoma Proteome Using Differential Scanning Calorimetry"** James Graham Brown Cancer Center Retreat: Fall 2014
  - Received Young Innovator in Roving Research Award
- Mary B. Hatch, Alagammai Kaliappan, Nick Allen, & Nichola Garbett. **"Calorimetry of the Plasma Proteome in Patients with Ovarian Cancer"** James Graham Brown Cancer Center Retreat: Fall 2014
- Manon G, Nick Allen, Alagammai Kaliappan, Nichola Garbett. **"Characterization of Plasma Thermogram Modulation using Mass Spectrometry"** James Graham Brown Cancer Center Retreat: Fall 2014
- Nick Allen, Joeseeph Tinney, Yuan Fangping, Bradley Keller, & Patricia Soucy. **"Exploring**

**Cardiac Fibroblasts in Different Media Conditions” UofL Summer 2013**

**Memberships and Service:**

- **Biomedical Engineering Society (Member: Fall 2012- present)**
  - **UL chapter Secretary : Summer 2013 – Spring 2014**
    - Maintain updated records for society on all social, fundraising and professional events
    - Worked with elective council to plan each semesters events and organized schedules to coordinate all events
  - **UL chapter Treasurer: Fall 2014**
    - Maintained financial records of all events planned for society
    - Collected local and national membership dues in accordance with BMES guidelines
    - Organized sending 3 UofL BMES members to national conference in San Antonio
- **Mortar Board National Honor Society (Member: Summer 2013- present)**
  - **Secretary: Fall 2014**
    - Maintained detailed meeting notes and assisted in organizing membership events
    - Proposed and developed plan for university wide academic hall of fame
- **Tutor for Upward Bound – ECTC (Spring 2012)**
  - Worked with local underprivileged high schools and tutored students in science and mathematics subjects
- **Phi-Theta Kappa National Community College Honor Society (Member: Fall 2011)**
- **Nominee for Golden Key National Honor Society**

**Awards and Honors:**

- Who’s Who Among American Colleges and Universities
- KCTCS All-Academic Team member
- KCTCS: Honors Award in Engineering
- Dean’s List (2010 – present) at both ECTC and U of L
- U of L Undergraduate Summer Research Grant awardee (Summer 2013)
- U of L Bioengineering Department: Judi Cooper Olsen Endowed Scholarship Award
- James Graham Brown Cancer Center: Young Innovator in Roving Research Award
- U of L Bioengineering Departmental Alumni Award
- U of L Ph. D Graduate Fellow